Performance of a Distensible-Tube Wave Attenuator in a Slender Focusing Channel

Antonio C. Mendes[1*], Francisco P. Braga[1] and John R. Chaplin[2]

[1]Laboratory of Fluid Mechanics and Turbomachinery, Electromechanical Engineering Department, Universidade da Beira Interior, 6201-001 Covilha, Portugal

[2]Emeritus Professor, Energy & Climate Change Research Group, Faculty of Engineering and Physical Sciences, University of Southampton, Southampton, U.K.

*Corresponding author. Email: acmendes@ubi.pt
Contributing authors: francisco.p.braga@ubi.pt, j.r.chaplin@soton.ac.uk

Abstract

A wave-energy device utilizing a water-filled distensible tube aligned head to waves is analysed. The wave-excited pressure bulges in the tube activate a stationary forward-bent circular oscillating water column (OWC) at its stern. This system has been extensively tested in wave-tank, at different scales. However, further improvements to its efficiency are possible. The present research assesses its performance at 1:20 scale, while operating in a slender focusing channel. Complementarily two other situations are considered: one at the nearshore, where the system is assembled to a bottom-standing jacket structure, and an onshore design where the tube operates in front of a sea wall in constant depth or over a sloping bottom. Deep and intermediate regular waves of small and finite amplitudes are generated in the wave-tank, representing the wave climate in the Occidental Group of the Azores islands. A non-linear power take-off impedance is imposed by a set of calibrated orifice plates and its characteristic is then obtained assuming compressible airflow. Measurements of air pressure in the pneumatic chamber, OWC free-surface displacement and incident wave-field provide estimates of energy capture-width, which are then compared with analytical predictions and benchmark test results. Photographs further help to understand the physics underlying the tube's working modes. Moreover, the performance of the system is obtained with and without the tube and then compared with standard values for OWCs. It is demonstrated that the addition of a distensible tube and a suitable focusing channel can significantly improve the capacity factor of a conventional OWC system.

Keywords: Ocean wave energy; Azores; Distensible tube; Focusing channel; Wave-tank tests.

Acknowledgments

The present study follows the work done under FCT Project PTDC/EME-MFE/111763, developed from 2012 to 2016 within the framework of the COMPETE Programme, partially funded by the Portuguese Foundation for Science and Technology and the European Union. The research was carried out in the experimental facilities of the Laboratory of Fluid Mechanics and Turbomachinery of Universidade da Beira Interior, in Portugal, with the collaboration of the University of Southampton in the UK. The authors are grateful to FCT and UBI for their support of the research activities. Furthermore, the valuable contribution of Mr. Morgado and of the Electromechanical Engineering Msc students that have helped to develop and assemble the experimental apparatus is acknowledged. The first author also wishes to acknowledge the valuable teachings of the late Professor Francis Farley, whose enthusiasm will always be remembered.

1 Introduction

In 2016 Steven Salter put forward a few thoughts concerning his more than 40 years of experience in the field of wave energy utilization. With the interest on renewable energy sources being nowadays more motivated by the growing problems of climate change and less by the possible shortage of fossil fuel supply, the target is still to design a cheap, efficient and resilient system, capable of withstanding harsh wave climates and of long-term operation without failure. However, this paradigm is strongly dependent on the international markets and energy policies in place. Besides all these aspects, Salter's (2016) insights are essential to the research and technological development of successful wave power conversion systems. A comprehensive review of the technologies developed until 2010 is given by Falcão (2010). Although by 2020 only the OWC type devices reached a technology readiness level (TRL) of 9, with a capacity factor of 25% (Magagna, 2020), there are a number of promising devices that are still under development. Inspired by the Dracones that were utilized in the 1950s for the transport of oil and also as protective barriers – a pioneer application patented by William Hawthorne and John Shaw in 1958 whose development is described in Hawthorne (1961) – Francis Farley and Rod Rainey patented in 2006 the Anaconda, a device that utilizes well-established rubber and turbine technologies (Farley and Rainey, 2006a). This concept makes use of a long rubber tube whose working principle relies on wave-excited pressure bulges to generate useful power. The electricity produced can then be fed to the grid ashore via a submarine cable. An independent analysis of the Anaconda done by the Carbon Trust in 2010 suggested it had the potential to deliver significant reductions in the cost of wave energy and, therefore, could belong to a future generation of ocean renewable energy converters.

Farley and Rainey (2006b) further on discuss some particularities of wave-profiling devices like the Anaconda. Its envisaged prototype consists of a water-filled rubber tube, 150 m in length and 7 m in diameter, floating freely head to waves. The up-wave end of the tube is closed and its stern may be connected to a power take-off (PTO) system. It was originally planned for deployment in water depths between 40 m and 100 m. Under operation the wave excited pressure pulses inside the tube grow in intensity as they travel in the downstream direction, with a speed that is governed by the tube's diameter and material properties. From the general theory for longitudinal waves in distensible tubes, developed in Lighthill (1978), it follows that resonance can be achieved if the celerity of the incident waves equals the speed of the internal pressure bulges. Therefore, tuning of such a device is a matter of choosing the adequate geometry, material properties and working pressure-head inside the tube. The first laboratory tests of the Anaconda were carried out by Chaplin et al. (2007a). The small-scale model was tested in a wave flume, submerged just below the still water line. Since the device was not fitted with any power take-off system, the wave energy it absorbed was in this case accounted for by hysteresis losses in the rubber and friction losses in the internal flow. The experiment provided an overestimated value of capture-width between 3 and 4 diameters. Based on the insights of this pioneering experiment, the working principle of the Anaconda wave power converter was reanalysed and discussed in detail in Chaplin et al. (2007b). A second series of tests were then performed with a 1:25 scale model of the Anaconda at the Offshore Wave Basin of the Danish Hydraulic Institute (DHI), in Denmark (Chaplin et al., 2010). The tests were essentially concerned with the measurement of outgoing waves that were radiated by the bulging tube. Two years later, Chaplin et al. (2012) report on results obtained with a linear pneumatic PTO of adjustable impedance, following an extensive series of experiments carried out at Solent University wave-tank in Southampton. A 1:25 scale tube made out of rubber and fabric was used, held fixed in both ends. For the first time theoretical predictions of power capture were found to be in close agreement with measurements obtained in linear wave conditions. Peak capture-widths were less than 2 tube diameters. In parallel Farley et al. (2012) give a comprehensive theory for distensible tubes operating in the sea, together with an assessment of the potential of a full-scale device, showing that the Anaconda belongs to a new class of competitive wave energy devices that are not yet fully developed.

Following earlier studies regarding an oscillating water column by Mendes and Monteiro (2007), Mendes et al. (2014) tackled the performance of a freely floating Anaconda working with a non-linear pneumatic power take-off system. The tube was in this case connected to a forward-bent circular OWC at its stern, whose pneumatic chamber connected to the atmosphere through a sharp-edged orifice. The performance assessment was based on a series of 1:100 scale model tests conducted in a wave flume, in regular waves of small and moderate amplitudes. Several calibrated orifices were used to emulate a non-linear pressure to volume flow-rate characteristic. As incompressible flow conditions were assumed, measurements of the wave-field as well as of the water-column oscillations in the vertical shaft delivered preliminary estimates of power output and energy capture efficiency. The results of this study clarified some previously unknown aspects of the system's behaviour, in deep as well as in intermediate water depth waves. In view of extending the former research,

a series of tests were then carried out with a 1:50 scale model in a wave-tank, clearly demonstrating the advantages of an adequate coupling between the tube and a forward-bent OWC (Mendes et al., 2017). The effects of model scale and air compressibility upon the capture-width were also considered and discussed. With a view to possibly harnessing wave power in the Azores, Mendes et al. (2020) later on focus on wave-tank tests of the OWC connected distensible tube, now at a larger 1:20 model scale. The tests were undertaken in regular waves that reproduced quite closely those encountered in the Azores Archipelago.

Before describing the present novel experiments, in which a distensible tube is placed in a converging channel, it is instructive to review earlier research on wave energy conversion under similar geometric conditions. An overview on theoretical investigations and model-scale testing of OWCs with projecting side-walls, having caisson and circular geometries, is next made. For a comprehensive review on OWC systems see Falcão and Henriques (2016). The inclusion of projecting side-walls in such systems brings significant advantages which should be clearly understood before adapting this solution to a distensible tube attenuator, an idea which is still under development. The use of projecting parallel walls was first proposed by Ambli et al. (1982) as part of the Kvaerner Multiresonant OWC project. They proposed adding parallel walls extending from the device towards the incident waves, in order to make use of the extra wave resonances that occur and contribute to increase the frequency bandwidth of maximum power extraction. The channel that was created generated an infinite series of resonant frequencies from which the quarter wavelength resonance is dominant. This increases the incident wave amplitude at the OWC mouth and thus the power available to be extracted over an extended frequency bandwidth. Two years later Count and Evans (1984) have confirmed theoretically, by two different approaches, that the addition of projecting side-walls to a caisson OWC is advantageous in increasing the device performance. They showed analytically and numerically that with carefully designed side-walls one may greatly increase its efficiency. Results are presented for the cases where the length of the projecting walls is equal or double the breadth of the OWC and compared with the case without the walls. Large wave amplifications between the walls are indeed achieved when the wavelength is four times the wall length. Additional resonances can also widen the favourable frequency bandwidth. The addition of the channel increases the efficiency and transports the maximum capture-width to larger wave periods; the longer the projecting walls the greater this shift is. Similar conclusions were extracted by Malmo and Reitan (1985) for an oscillating water column of caisson geometry, placed between projecting side-walls in a channel, by modelling the flow in linear theory. One year later the authors extended this study to consider only the case of an OWC in a reflecting wall (Malmo and Reitan, 1986). Also using linear theory, McIver and Evans (1988) later analysed the performance of caisson OWCs imbedded on a reflecting wall at constant depth. Firstly they considered the influence of the wall length to width ratio on a single device, concluding that as this ratio increases the maximum capture-width also increases; however, its bandwidth of high efficiency decreases. Vice-versa, a wider and shorter channel reduces the maximum capture, but widens the bandwidth. An important feature that may result from the coupling between the flow at the channel mouth and the working mode of the device is the shift of the maximum capture-widths to longer wave periods, thus enabling the design of smaller devices. They also demonstrated the benefits brought forth by having a number of neighbouring devices instead of an isolated one. For the case of a series of rectangular channel OWCs that are imbedded, equally spaced in a seawall, the maximum power that can be absorbed depends only on the position of the channel mouths and wavelength. Channel spacing can then be chosen without the details of the device or projecting wall characteristics. The inclusion of converging sidewalls further concentrates the incident wave energy into the device as was fully demonstrated experimentally by Whittaker and Stewart (1993), by means of a series of radiation tests conducted for a nearshore and shoreline OWC. They have tested the following configurations of OWC: an isolated caisson with and without parallel or flared walls, and the cases where the OWC has a reflecting wall or where the harbour is imbedded in a coastline. They demonstrate that the maximum capture-width of an isolated OWC with a harbour of parallel walls is practically the same as that of a single isolated OWC. By adding a reflecting wall the capture-width is doubled and with flared projecting walls the capture further increases significantly. The mechanism of the hydrodynamic interactions leading to the amplification of the excitation force and the resulting improvement of the power extraction are well described by these authors. They explain that for a nearshore device with parallel projecting side-walls, the wave amplitude in the harbour is maximum at its fundamental resonant frequency, thus yielding a maximum excitation force. This happens because the radiation damping is a maximum at the fundamental harbour resonant frequency. This resonance occurs when the effective length of the harbour is precisely one quarter of the wavelength. The system with a harbour of parallel walls is in fact multi-resonant; the resonant frequencies depend on the length of the harbour and the extent to which they influence the performance is determined by the level of applied damping. The use of convergent side-walls, on the other hand, allows the physical dimensions of the OWC to be reduced while maintaining an acceptable performance. More recently, Tseng et al. (2000) tested a 1:20 scale model of a bottom-standing vertical circular OWC of 0.6 m diameter, having projecting walls with a 60° opening at its entrance and an arc-shaped lip, aiming to match the wave climate in Taiwan. The focusing channel

length to OWC diameter ratio was 0.8. The tests were carried out in wave-tank under intermediate waves in $0.6\,m$ water depth, having periods $T = 1.34 - 2.68$ s and wave steepness $H/\lambda = 0.0081 - 0.0395$. The authors shed light on the energy transformation possess, providing an assessment of the device hydrodynamic and overall efficiencies. An energy balance indicates that only 28.5% of the incident-wave energy was converted into pneumatic energy, due to the high level of losses. In order to examine the performance of a bottom-standing vertical circular OWC installed at the tip of a wedge shaped coast line, Lovas et al. (2010) later extended the linear analytical model of Martins-Rivas and Mei (2009) developed for a single fixed draft OWC at the tip of a thin breakwater. Both the concave and convex corner cases are studied and compared with the straight coastline case, the concave geometry being similar to a focusing channel with walls of infinite length. It was found that as the opening angle of the focusing channel decreases, more wave energy is channelled towards the OWC and less is lost by radiation. As such, the efficiency of the system installed at a concave corner is significantly greater than in the other two geometries and about 4 times greater than the single OWC in a thin breakwater. Deng et al. (2014) afterwards analysed a bottom-standing circular OWC with a flared V-shaped channel of finite length at its mouth, by means of a theoretical model based on linear theory. The effects of channel length and opening angle were explored. As expected, the projecting sidewalls increase the performance of the OWC system significantly. The finite length V-shaped channel was in this case able to improve the energy conversion efficiency up to three times and to widen its bandwidth. They showed that the ideal opening angle between the channel sidewalls should be between 90° and 135°. However their results seem to exhibit a trend where, for longer channels, a better efficiency is achieved with a smaller opening angle. In terms of capture-width, the OWC-type device with a V-shaped channel is about two to three times more efficient than the one studied by the same author without the projecting walls (Deng et al., 2013). Interestingly, the infinite length walls considered in Lovas et al. (2010) lead to an increase of capture-width of 4 times, while the finite length walls of Deng et al. (2014) lead to an increase of up to 3 times. David et al. (2018) also tested the influence of the projecting sidewalls length and their opening angle on the hydrodynamic efficiency, but now for a caisson OWC in shallow water of constant depth. They claimed that, although the addition of projecting walls at uniform depth had no significant influence on the efficiency toward the low-frequency range, the deployment of such an OWC device incorporated in a breakwater could be an economically viable solution. An optimal relation between the channel length and the breadth of the OWC caisson has been found by these authors, which is in close agreement with the range suggested by Deng et al. (2014) for circular OWCs.

In view of improving the performance of the distensible tube wave attenuator for operation in the Azores, the present research extends the experiments earlier conducted at 1:20 model scale to consider its operation at the nearshore in water depths up to 50 m. At full scale the distensible tubes envisaged would have a length between 34 m and 43 m, with a diameter of about 7 m. Two different situations are studied: one where the system is assembled to a bottom standing jacket structure nearshore and an onshore design where the tube operates in a focusing channel. Measurements of the internal OWC free-surface displacement, pressure in the pneumatic chamber and incident wave field were carried out. As to obtain estimates of the system's extracted power and energy capture-width under the different wave loading conditions imposed, non-linear pressure to volume flow characteristic curves were determined which are in practice similar to the ones typical of impulse air turbines. The accuracy of such estimates is however greatly dependent on the volume-flow calculations. Therefore, taking into account air compressibility, the flow-rate is herein derived from the energy equation for adiabatic flow. The inherent discharge coefficient of the orifice flow is iteratively obtained using Miller's algorithm (Miller, 1996). The dynamics of the system are subsequently analysed in terms of an amplification factor and the physics underlying the tube's working modes in surge, bulging and bending were captured in a set of images recorded by a submersible camera.

The capture-width obtained in the present experiment is validated against benchmark test results given in Chaplin et al. (2012). The performance with a distensible tube in place is next compared with the corresponding output without the tube. For the case of the forward-bent OWC, without the tube, its performance is equally compared with experimental, analytical and numerical data available in the literature for fixed draft and bottom standing OWCs, with and without projecting side-walls. All in all, the benefits of a reflecting sea-wall are put in evidence as well as of the resonant modes introduced by a focusing channel. A comparison between the capture-width envelopes of the considered situations, as a function of the full-scale significant wave period, leads to the conclusion that a freely floating tube is adapted for shorter wavelengths in the offshore. Instead, a focusing channel is as expected more suited for nearshore and onshore applications, with longer waves. It is demonstrated that the addition of a slender focusing channel to the distensible-tube can significantly enhance the capacity factor of the system.

2 Experimental setup

For reference purposes, experiments were first carried out in a channel of constant cross-section. The prototype of the distensible-tube wave attenuator is foreseen to have a long rubber tube of about 7 m in diameter, operating in deep and intermediate waves at water depths under 50 m. A model of this device was tested at a scale of 1:20 in an 11 m long and $b = 2.06$ m wide wave-tank, equipped with a paddle-type wave maker driven by a DC electrical motor and an absorbing beach of 16° slope, at opposite ends. The water depth in the tank was $h = 1.9$ m. The experimental arrangement firstly considers the situation of a nearshore system, where the tube is mounted on a bottom standing jacket structure and interacts with incident regular waves (configuration A, shown in fig. 1a). It comprises a latex tube with $L = 2.15$ m in length, pressurized diameter $d = 0.348$ m and wall thickness $w = 2$ mm. At its stern the tube is connected to a vertical acrylic duct through a PVC elbow, at a depth a of 8.5 cm (fig. 1b). The other end of the rubber tube is closed by a floating wooden nose that accommodates a plastic hose connected to a pump for the purpose of pressurising the tube. This hose also acts as a mooring for the tube. The operating internal head at the vertical duct was $h_0 = 29.6$ cm, at which pressure the rubber tube was tuned to incident waves of period $T = 1.5$ s.

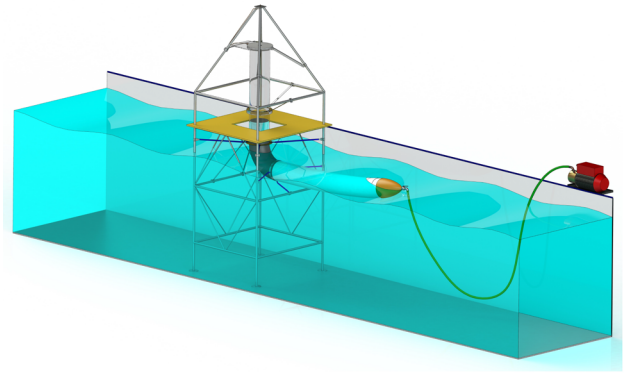

(a)

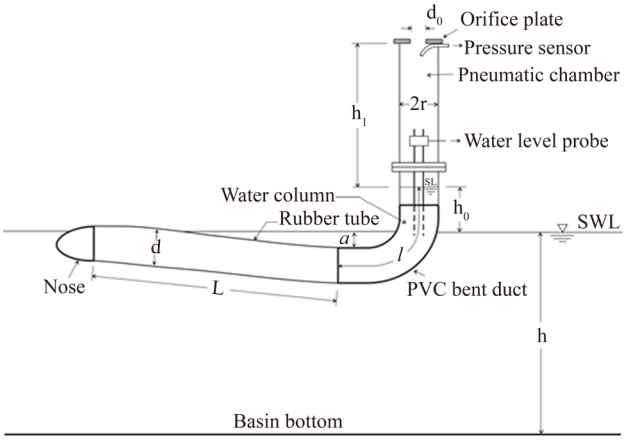

(b)

Fig. 1 1:20 scale physical model of the nearshore distensible-tube wave attenuator in the wave-tank (configuration A)

For this configuration (denoted A), the forward-bent circular OWC was held in position by means of a jacket structure which supports a platform located 2.32 m above the wave-tank floor with a square hole at its centre, to accommodate the vertical

shaft containing the OWC and pneumatic chamber. The pneumatic power take-off system consists of an air chamber of diameter $2r = 28.9$ cm and height $h_1 = 1.42$ m when the water-column is at rest, connecting to the atmosphere through a sharp-edged orifice plate of diameter d_0. When under the action of the water piston, the variation of the pressure in the chamber forces the air through the orifice. Several calibrated orifices of different diameters between $d_0 = 15$ and 60 mm were tested. In tables 1 and 2 the relevant dimensions of the physical model and PTO system are presented.

Subsequently the system was modified in order to investigate the operation of the device in three onshore configurations. In configuration B the cross section of the channel remained the same, but it was fitted with a vertical barrier that extended from the bottom up to the free surface. In configuration C the side walls of the channel remained parallel and the barrier remained in place, but the floor sloped upwards. Finally in configuration D, sketched in Fig. 2(a), the floor was sloping and the side walls converged. In all cases the OWC system was installed behind the barrier. In these configurations the length of the latex tube was $L = 1.71$ m, its wall thickness was $w = 2$ mm and the pressure head $h_0 = 24.6$ cm delivered a pressurized tube diameter d of about 0.35 m. The bulge wave tuning period is again $T_1 = 1.5$ s. The height of the pneumatic chamber is in these configurations $h_1 = 1.469$ m and the orifice diameters d_0 cover a range of 20 mm to 50 mm. A straight PVC pipe section had to be added to the elbow in order to meet the rubber tube at the vertical wall, thus increasing the OWC length l in relation to configuration A. All the relevant dimensions of the four configurations tested are presented in tables 1 and 2. At rest the volume of the pneumatic chamber varied from 93 dm^3 to 96 dm^3, depending on the situation, which is still not sufficient to guarantee similarity of the elastic forces between model and prototype. Additional reservoirs were not used, as this would alter the Reynolds number of the orifice flow significantly, thus leading to further difficulties in achieving similarity between model and prototype.

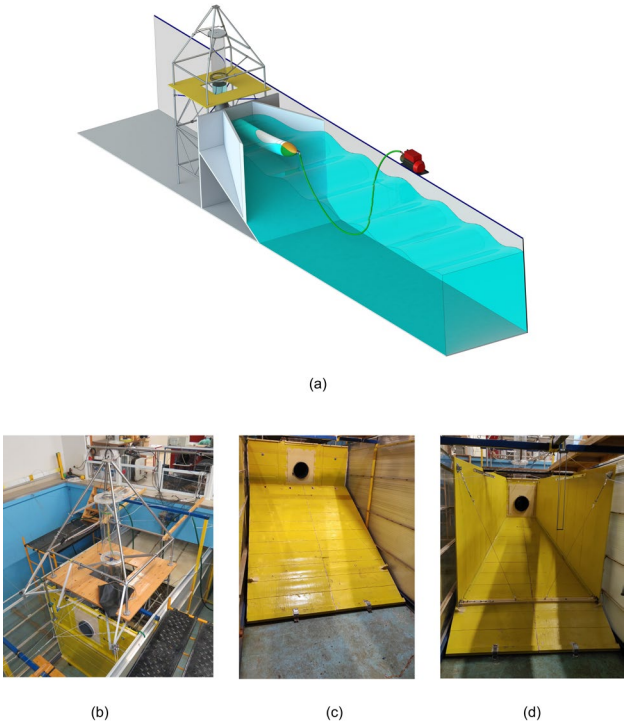

Fig. 2 Representation of the onshore system: a) system in a focusing channel (Configuration D); b) reflecting barrier; c) barrier with a sloping bottom; d) focusing channel

Table 1 Dimensions of the OWC and pneumatic power take-off system

Config.	$2r$ (cm)	l (m)	h_1 (m)	d_0 (mm)
A	28.9	0.76	1.419	20 – 60
B	28.9	1.11	1.469	20 – 50
C	28.9	1.11	1.469	15 – 37.4
D	28.9	1.11	1.469	15 – 37.4

Table 2 Rubber tube dimensions, stern submergence and pressure head

Config.	L (m)	d (cm)	w (mm)	a (cm)	h_0 (cm)
A	2.15	34.8	2	8.5	29.6
B	1.71	35.1	2	8.5	24.6
C	1.71	35.1	2	8.5	24.6
D	1.71	35.2	2	8.5	24.6

The focusing channel that was assembled at the end of the rectangular wave-tank, in front of the jacket platform, is shown in fig. 3. The channel is $X = 1.846$ m long, with a mouth 1.9 m wide, whose side walls converge into a reflecting wall where they define a 0.645 m by 0.555 m rectangular surface pierced by the OWC mouth. The channel side walls run along a $29.1°$ slopping bottom and have a flare angle $\theta = 37.54°$. The sloping-bottom has a horizontal length $X_S = 2.415$ m. A small gap $e = 6.5$ cm exists between the channel mouth and the tank side-walls. Inside the focusing channel a 1.71 m long rubber tube is connected to the OWC mouth, whose top is submerged $a = 8.5$ cm beneath the still water line. Fig. 4 details the precise dimensions of configurations B, C and D.

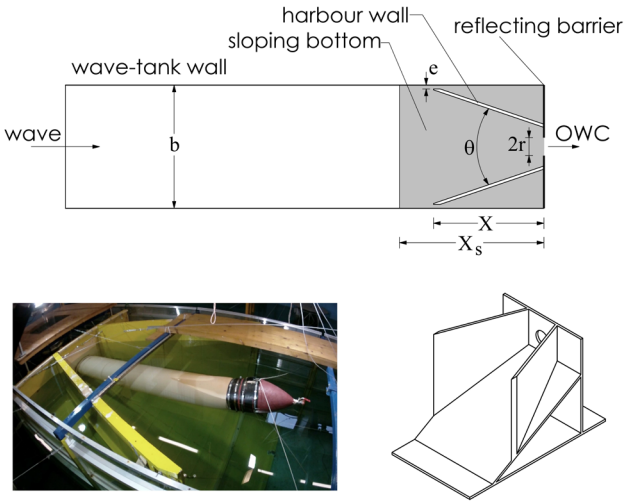

Fig. 3 Complete physical model of the distensible tube system (configuration D)

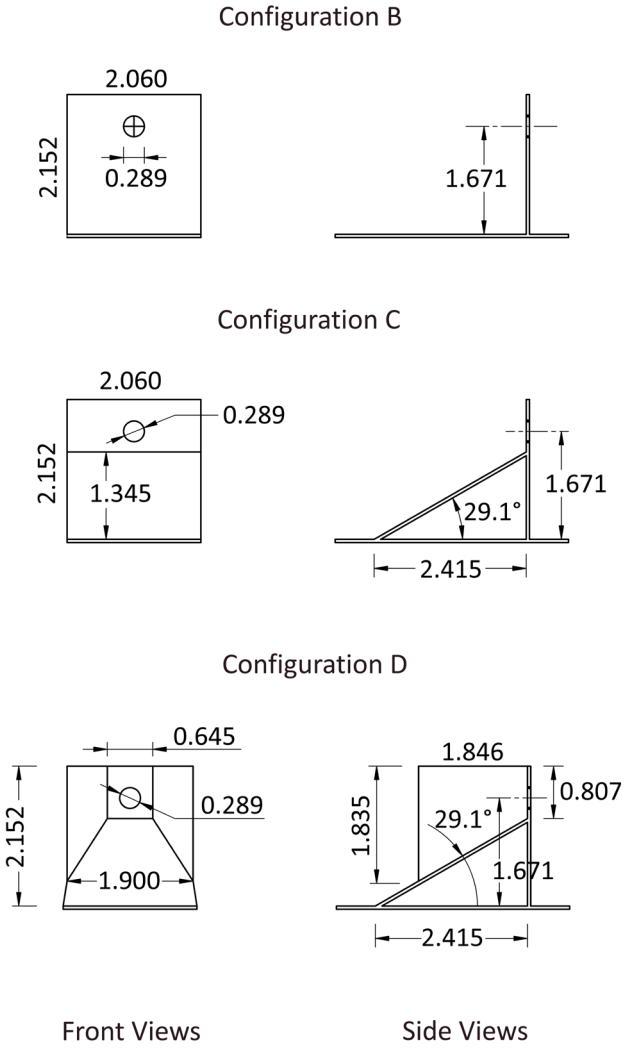

Fig. 4 Detailed drawings with dimensions in m of the barrier used in configuration B, barrier with sloping bottom of configuration C and focusing channel of configuration D

A wave probe monitoring system from Wallingford provided recordings of the OWC surface displacement, and similar wave gauges recorded the wave surface elevation at three points between the model and the wave generator for the purpose of identifying wave reflections following Mansard and Funke (1980). The pressure in the pneumatic chamber was measured by a pressure transducer PX409-005CGV, from OMEGA, with a stated accuracy of $\pm 0.08\%\ BSL\ LHR$. All measurements are collected by a KUSB-3100 S data acquisition module from Keithley at a rate of 200 Hz for 30 seconds, with a separation of less than one micro-second between adjacent channels.

3 Wave conditions at model scale

The Azores are a group of nine islands located in the Mid Atlantic Ridge, belonging to the Macaronesia. They are of particular interest for wave power harnessing due to the highly energetic wave climate and steep seabed slopes. Sometimes, there can even be a natural focussing effect that may be beneficial for wave energy harnessing, like in the case of the PICO power plant at Porto Cachorro (Sarmento et al., 2003). An assessment of wave directionality, mean wave period and significant wave height in the Azores was facilitated by Histograms gathered by Caires et al. (2013) at KNMI (the Royal Meteorologic Institute of the Netherlands); they are based on 45 years of reanalysis data of deep-water waves from the ERA-40 model of the European Center for Medium Range Weather Forecasts (ECMWF). Fig. 5 presents the data collected for a region comprised between 27°N – 45°N latitude and 36°E – 18°E longitude. This area encompasses the entire Exclusive Economic Zone of the Azores. It may be seen that 28.6% of the total number of observed waves come from W to NW and 27.2% come from NW to N. The number of waves arriving from directions between East and South-West is not significant and amounts to less than 8% of the observations. Essentially the mean periods range from 5 s to 10 s, with significant wave heights up to 6 m. The first islands encountered by the predominant waves are Flores and Corvo which belong to the occidental group of the archipelago. Taking Corvo island in the Azores archipelago as a case study, depths between 20 m and 50 m can be found at a distance roughly between 0.68 km and 1.30 km off the western coast of the island. Comparable water depths can be found closer to the eastern coast, roughly between 0.38 km and 0.90 km. According to Matos et al. (2015), the mean wave energy potential available at Corvo Island is the largest of the archipelago. This is in accordance with the predominant incident wave direction and to the absence of land masses upstream of the island. Its western coast has an average energy potential between 70 and 110 kW/m, while the East coast has only 50 to 80 kW/m. It is worth mentioning that the peak wave periods can even be larger in the island's shadow, with more amenable wave heights, pointing to a much less harsh wave climate in this area, especially during winter. The seasonality between the summer and winter months is significant.

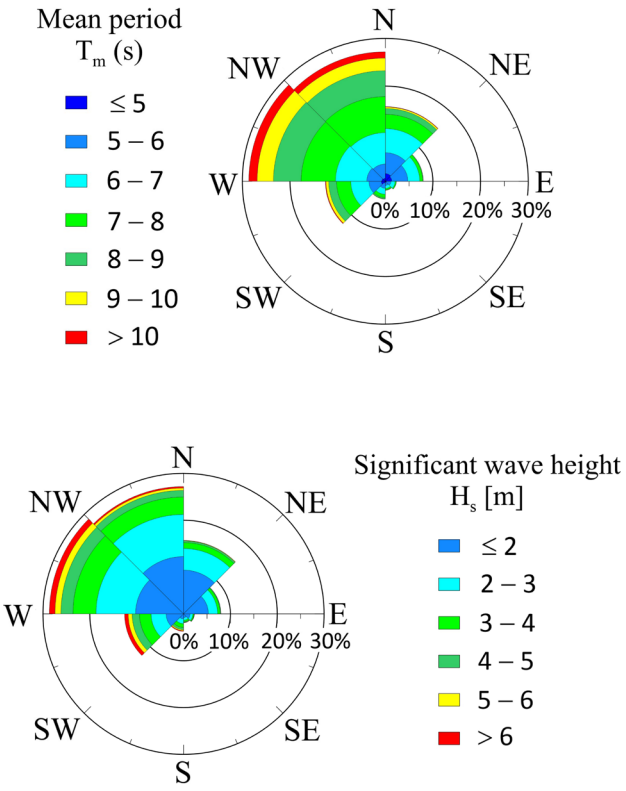

Fig. 5 Percentual observations of wave directionality in the Azores region (Lat: 27°N – 45°N; Lon: 36°E – 18°E): directionality and mean period (top); directionality and significant wave height (bottom)

Table 3 shows the incident waves generated in the wave-tank for all the configurations tested at model scale. The relevant parameters are the wave period T, the fundamental wavenumber k, the wave height H, the wave steepness H/λ, the relative water-depth h/λ, the celerity of the waves c, the Ursel Number Ur and the incident wave power P_i per unit wave front.

Table 3 Incident wave-field generated at model scale

Config.	T (s)	$k(\mathrm{m}^{-1})$	H (cm)	H/λ
A	1.06–1.96	1.08–3.61	6.7–23.4	0.01–0.12
B	1.14–2.50	0.73–3.12	4.0–18.8	0.01–0.09
C	1.15–2.49	0.73–3.02	3.8–15.8	0.01–0.07
D	1.11–2.51	0.73–3.29	3.9–19.1	0.01–0.09
Config.	h/λ	c (m/s)	Ur	P_i (W/m)
A	0.18–1.09	1.65–2.97	0.06–0.42	9.03–58.40
B	0.22–0.94	1.77–3.45	0.07–0.73	5.53–63.83
C	0.22–0.91	1.80–3.44	0.05–0.74	3.69–65.58
D	0.22–1.00	1.73–3.46	0.06–0.70	5.24–58.54

4 System dynamics and tuning

A general theory for wave propagation in a distensible tube is given in Lighthill (1976), with additions for present purposes by Farley et al. (2012). In the current device the surge, bending and bulging working modes of a distensible tube are coupled to excite the oscillations of a water column. In the absence of hysteresis, the bulge-wave speed inside the tube is $U = 1/\sqrt{\rho_1 D}$, where ρ_1 is the mass density of water and D is the distensibility of the tube. For a circular tube with diameter d and wall-thickness w, $D = d/(wE)$; here E is the Young's modulus of latex (approximately 0.91 MPa at 100% strain). Therefore, the bulge speed in the tube is:

$$U = \sqrt{\frac{wE}{\rho_1 d}} \tag{1}$$

In the present case, for which the tube's mean diameter is $d = 34.8$ cm and its wall thickness is $w = 2$ mm, the free bulge wave speed is $U = 2.29$ m/s at model scale. This matches the celerity of waves of period $T_1 = 1.47$ s. At such a period, waves in the tank would be propagating in deep-water conditions. At full-scale this state of affairs corresponds to waves with periods of approximately 6.5 s and wavelength 67 m, propagating in a water depth of 38 m.

The pneumatic power take-off system is activated by the oscillations of the water column in the vertical duct which, in turn, are excited by the longitudinal waves in the rubber tube. From actual measurements conducted with the OWC shaft open, the natural period of this system is $T_0 = 1.75$ s. This happens to be very close to the resonant period calculated for a water column of length l, this dimension being determined by the length of the bent duct plus the static head h_0 (see fig. 1b). The OWC will then resonate at a full-scale wave period of 7.83 s. A water column capable of generating the desired resonant conditions would be roughly 15.2 m in length; of these, 5.9 m emerge above the still water line to provide the static pressure head h_0.

5 Air volume-flow estimates

The pneumatic power take-off consists of a set of orifice plates with calibrated diameters d_0 between 15 mm and 60 mm (fig. 6). Estimates of power and energy capture are greatly dependent on the accuracy of the calculated air flow-rate across the orifice. For this reason care was taken to calculate the flow as accurately as possible, and different methods have been used for the purpose of increasing its reliability, as described in Reader-Harris (2015).

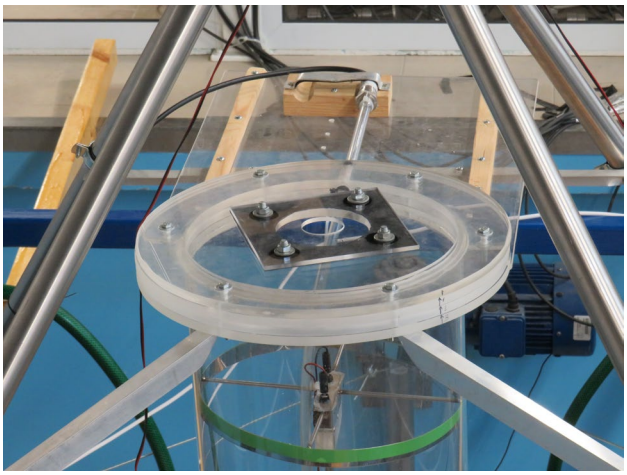

Fig. 6 Orifice flow pneumatic power take-off

The air mass flow-rate across the orifice $\dot{m}$ may be obtained from the energy equation for steady uniform flow and the law of mass conservation for compressible flow. As the pressure p changes in the pneumatic chamber, the mass-density ρ of air passing through the orifice of diameter d_0 also changes. If the pressure variations occur quickly the process may be assumed adiabatic and, for an ideal gas, the expansion process is isentropic. By using the adiabatic relation $p/\rho^{\gamma} = constant$ with $\gamma = 1.4$, we get:

$$\dot{m} = \frac{\varepsilon}{\sqrt{1 - \beta^4}} \frac{\pi d_0^2}{4} \sqrt{2\,\rho^*\,\Delta p} \tag{2}$$

In this expression Δp is the differential pressure between the pneumatic chamber and the atmosphere; it is $\Delta p = p - p_0$ when the air exits the chamber (outflow) and $\Delta p = p_0 - p$ when it enters (inflow). The mass density of air upstream of the orifice is ρ^*, β is the orifice diameter to upstream reference diameter ratio and ε is the well-known expansibility factor. The effect of ε is to reduce the air mass flow-rate across the orifice. This factor takes the value 1 when the flow is incompressible; otherwise for compressible flow, taking $n = p_0/p$ in the outflow case and $n = p/p_0$ in the inflow case, it is given by:

$$\varepsilon = \sqrt{\left(\frac{\gamma n^{2/\gamma}}{\gamma - 1}\right)\left(\frac{1 - \beta^4}{1 - \beta^4 n^{2/\gamma}}\right)\left(\frac{1 - n^{\frac{\gamma-1}{\gamma}}}{1 - n}\right)} \tag{3}$$

For orifice flow the expansibility factor ε has to be determined experimentally. An empirical formula is used in the present case, taken from ASME MFC-3M-1989 standards, later revised in ASME (2004):

$$\varepsilon = 1 - \gamma^{-1}\,(0.41 + 0.35\,\beta^4)(\Delta p/p^*) \tag{4}$$

where p^* denotes the air pressure upstream of the orifice. The volume flow across the orifice Q may be derived from eq. (2), taking $Q = \dot{m}/\rho^*$.

Fig. 7 shows a 5 second time series of the expansibility factor ε calculated from eq. (4), together with the pressure in the pneumatic chamber p and the OWC displacement η, for the system in configuration A with a PTO orifice of $d_0 = 30$ mm and an incident wave period $T = 1.17$ s; the wave height is $H = 9.93$ cm and the wavelength is $\lambda = 2.13$ m. As Δp and the volume-flow augment the expansibility factor decreases, whereas the opposite happens when Δp decreases. Whenever the OWC displacement reaches its maximum or minimum points, the mass flow-rate is 0 and the expansibility factor equals 1. The greater the pressure differential Δp, the smaller is ε and the more the flow-rate is reduced by it, at most 0.5% ($\varepsilon = 0.995$). These results were derived from the measured time series, considering all their frequency components.

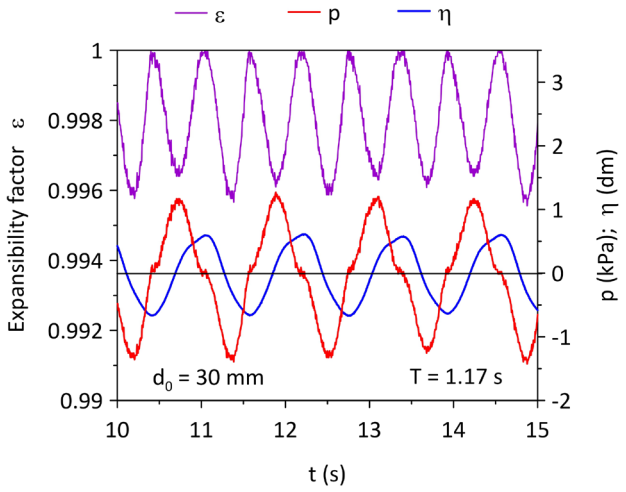

Fig. 7 5-sec time series of the expansibility factor ε obtained from eq. (4), together with the relative pressure in the pneumatic chamber p and the OWC displacement η, for the system in Configuration A with a PTO orifice of $d_0 = 30$ mm under incident waves of period $T = 1.17$ s

It is important to note that the expression for the mass flow-rate across the orifice of eq. (2) is still incomplete. This derives from the fact that there is a pressure-loss due to friction at the orifice. In order to account for this loss and for the *Vena-contracta*, the mass flow-rate still has to be multiplied by a discharge coefficient C_d. The complete equation for the mass flow-rate across the PTO orifice therefore is:

$$\dot{m} = C_d \frac{\varepsilon}{\sqrt{1 - \beta^4}} \frac{\pi d_0^2}{4} \sqrt{2\,\rho^* \Delta p} \tag{5}$$

The value for the discharge coefficient C_d that is normally assumed for sharp-edged orifice flows is of around 0.6. However, as its exact value depends on the Reynolds number various empirical equations have been derived to determine C_d. In the present case an algorithm for compressible flow presented in Miller (1996) has been applied to iteratively determine the discharge coefficient and thus reduce the uncertainty of the volume flow calculations across the PTO orifice. For turbulent flow of Reynolds number $Re > 4000$, the discharge coefficient can be expressed as:

$$C_d = C_\infty + \frac{b'}{(Re_u)^{0.75}} \tag{6}$$

where Re_u is the Reynolds Number referred to the velocity upstream of the orifice and b' is the Reynolds correction factor. C_∞ is the discharge coefficient for an infinite Reynolds Number which, for flange tapings and $r > 29.2$ mm is:

$$C_\infty = 0.5959 + 0.0312\,\beta^{2.1} - 0.184\,\beta^8 + 2.286 \frac{\beta^4}{2r(1 - \beta^4)} - 0.856 \frac{\beta^3}{2r} \tag{7}$$

Here $2r = 289$ mm. The Reynolds correction factor is, on the other hand:

$$b' = 91.706\,\beta^{2.5} \tag{8}$$

It should be noted that there is an asymmetry when the air flows into or out of the pneumatic chamber, depending on the sign of $p - p_0$. In the previous equations $Re_u = (2\rho^* Q)/(\pi\mu r)$ and $\beta = d_0/2r$ when the pneumatic chamber delivers air to the atmosphere; μ is the absolute viscosity of air. Otherwise, when the pneumatic chamber sucks air from the atmosphere, it is assumed that the air flows from a reservoir whose diameter is 100 times larger than d_0. In this case $\beta = 0.01$ and $Re_u = \rho^* Q/(25\pi\mu d_0)$. This assumption is compatible with the existence of stagnation conditions outside the pneumatic chamber.

The discharge coefficient C_d being directly dependent on the Reynolds Number, it is necessary to iterate eqs. (5) and (6) to get a good approximation of $\dot{m}$. The following steps where undertaken:

1. A first approximation of $\dot{m}$ is obtained assuming a value of C_d between 0 and 1 in eq. (5);
2. With the previous approximation of $\dot{m}$ the Reynolds number upstream Re_u is calculated;
3. From the previous value of Re_u a new C_d is obtained from eq. (6);
4. The new C_d gives an updated value of $\dot{m}$ from eq. (5);
5. The procedure loops back to step 2 until convergence is attained.

In fig. 8 the values of C_d obtained from Miller's algorithm are presented and compared to the standard value of $C_d = 0.6$, for the system in Configuration A with a PTO orifice of $d_0 = 30$ mm under incident waves of period $T = 1.17$ s. The percentage deviation in the volume-flow caused by these two approaches is below 0.7% for $Re = 3.67 \times 10^4$, as summarized in table 4. As expected, both instantaneous values of the iterative C_d and of the expansibility factor ε reflect the asymmetry of the airflow inhalation and exhalation.

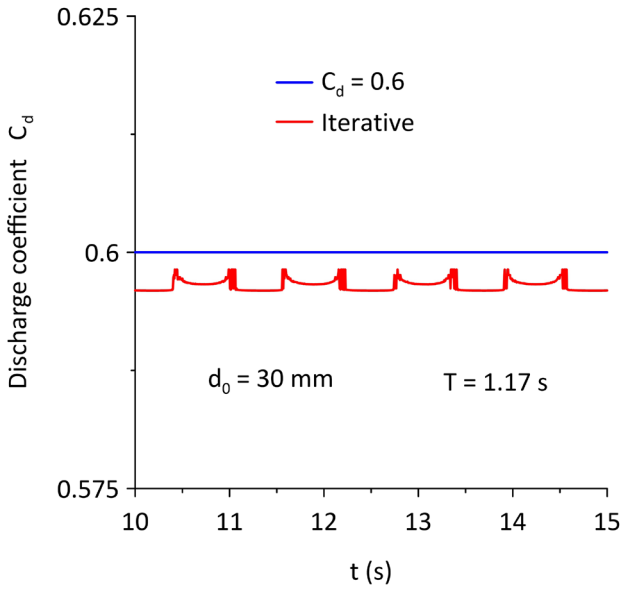

Fig. 8 5-sec time series of the orifice discharge coefficient C_d obtained from eq. (6), for the system in Configuration A with a PTO orifice of $d_0 = 30$ mm, under incident waves of period $T = 1.17$ s

Table 4 Percentual deviation between the air volume flow calculated assuming a fixed $C_d = 0.6$ and an iterative C_d (Miller, 1996)

d_0 (mm)	T (s)	Mean Re	Deviation (%)
30	1.17	3.67×10^4	0.3 – 0.7

6 Mean extracted power and efficiency

If $p(t)$ is the measured air pressure in the pneumatic chamber at time t, the instantaneous power extracted by the PTO is for compressible flow:

$$P(t) = \frac{\dot{m}}{\rho^*} \Delta p \tag{9}$$

where $\Delta p = |p - p_0|$, the instantaneous air mass-flow $\dot{m}$ is given by eq. (5) and ρ^* is the instantaneous mass density upstream of the orifice, obtained from the adiabatic relation. The mean power $\bar{P}$ extracted in a wave cycle T is then:

$$\bar{P} = \frac{1}{T} \int_0^T \frac{\Delta p(t)}{\rho^*} \dot{m}(t) \; dt \tag{10}$$

The energy extraction efficiency of the system may now be conveniently expressed, in tube diameters, by means of an energy capture-width C_W defined as follows:

$$C_W = \frac{\bar{P}}{P_i \times d} \tag{11}$$

where P_i is the incident wave power per unit wave front and d is in this case the diameter of the pressurized rubber tube.

Based on the methodology described above, fig. 9 depicts a 5-sec record of the instantaneous pneumatic chamber pressure p and volume-flow Q for the system in Configuration A with a PTO orifice of $d_0 = 30$ mm, under incident waves of period $T = 1.17$ s. The corresponding instantaneous extracted power P and mean power $\bar{P}$ extracted at the orifice are also represented. In these conditions the wavelength is equal to the tube's length ($\lambda = L$), a circumstance that strongly influences the system's efficiency in this configuration, as will be seen later on.

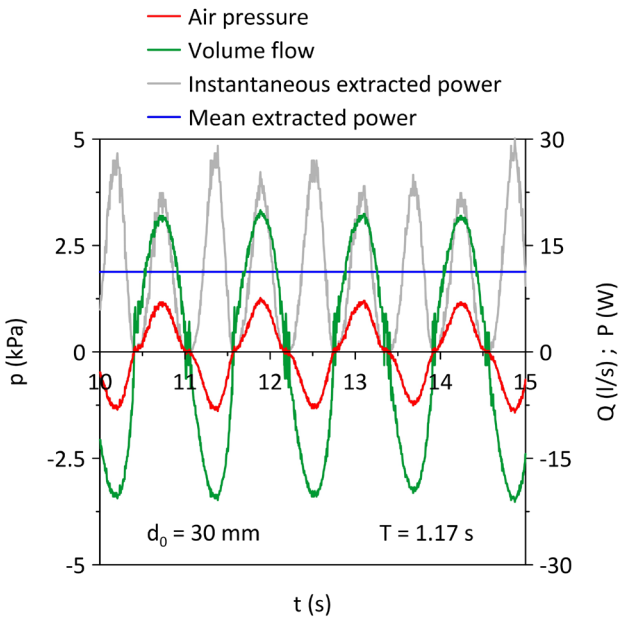

Fig. 9 5-sec time series of measured relative pressure in the pneumatic chamber p, calculated air volume flow Q, instantaneous extracted power P and mean power $\bar{P}$, for the system in Configuration A with a PTO orifice of $d_0 =$ 30 mm, under incident waves of period $T = 1.17$ s

The pressure to volume-flow characteristic of the PTO orifices is given in fig. 10, for all the configurations and wave loading conditions imposed. The experimental data fits a quadratic characteristic typical of impulse air turbines with a correlation coefficient between 0.98 and 0.99. The PTO characteristic is seen to be independent of the wave steepness.

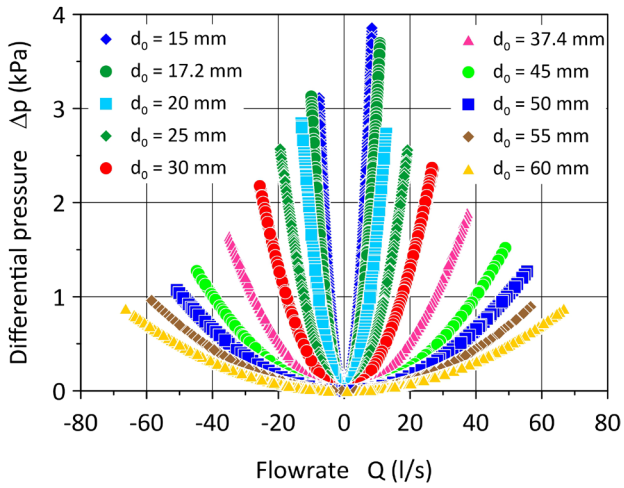

Fig. 10 Pressure to volume-flow characteristic of the PTO orifices, for all the configurations and wave loading conditions imposed

An important property to be found is the power take-off system impedance. Assuming the characteristic of the orifice of area A_0 is $Q = C_0 A_0 \sqrt{\Delta p/\rho^*}$, with C_0 being a dimensionless coefficient, then the PTO impedance – pressure difference divided by the flow-rate – is $\rho^* Q/(C_0 A_0)^2$. This clearly varies through the wave cycle, and assuming it follows a sinusoidal variation then the mean PTO impedance $\bar{Z}_{PTO}$ [kPa m^{-3} s] is:

$$\bar{Z}_{PTO} = \frac{2\rho^* q}{\pi {A_0}^2 C_0^2} \tag{12}$$

where q is the maximum instantaneous volume flow-rate.

The impedance coefficient C_0 can be obtained from the orifice characteristic as $C_0 = Q/\left(A_0\sqrt{\Delta p/\rho^*}\right)$, by using the measured differential pressure in the pneumatic chamber Δp and the volume-flow Q, calculated for each time series. If all the frequency components of the time series are considered, the coefficient C_0 is not constant in a wave cycle and a mean value must be taken.

Furthermore a normalized impedance $Z = \bar{Z}_{PTO} \,/\, Z_{tube}$ is defined, which is useful in the case of an OWC system connected to a distensible tube. The inherent impedance of the tube Z_{tube} is:

$$Z_{tube} = \frac{\rho_1 U}{\left(\frac{\pi d^2}{4}\right)} \tag{13}$$

where ρ_1 is the mass density of water and $U = 1/\sqrt{D\,\rho_1}$ is the bulge-wave speed in the tube, in the absence of hysteresis; D is the tube's distensibility and E is the Young's modulus of the rubber. The normalized impedance Z is useful when assessing its influence on the system's performance and later on for comparing with benchmark results.

7 The nearshore system

In the nearshore system (configuration A) the tube is connected to a forward-bent OWC, which is held in place by a bottom standing jacket platform. In fig. 11 its amplification factor ζ, defined as the ratio of the OWC displacement height to incident wave height, is presented as a function of the normalized wave period T/T_1 for a freely floating 2.15 m long rubber tube having a pressurized diameter of 34.8 cm. The chart shows the results obtained for eight different PTO orifice diameters, between 20 and 60 mm, as well as for the undamped case where the pneumatic chamber is completely open to the atmosphere. In this configuration ζ is maximum at the OWC resonance ($T = 1.75$ s), quite close to where the wavelength is twice the tube's length ($T = 1.67$ s). It reaches 5.4 for $d_0 = 60$ mm and 7.7 for the open shaft. No significant amplification peak is apparent in the vicinity of the tube tunning period ($T = 1.47$ s). However, the value of ζ is here comparable to the one achieved when the wavelength matches the tube length ($\lambda = L$), reaching 2.2 for $T = 1.19$ s.

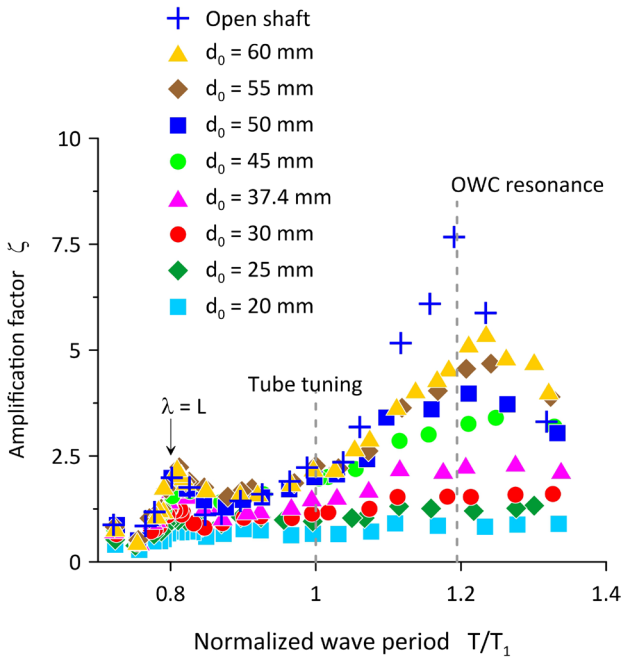

Fig. 11 Amplification factor ζ as a function of the normalized wave period T/T_1, for the system with the tube assembled to a jacket platform over uniform depth (configuration A) and all the PTO impedance rates tested, including the undamped case

Fig. 12 shows the power capture-width C_W as a function of the normalized wave period T/T_1. C_W reaches about 2 tube diameters at the OWC resonance ($T = 1.75$ s), a local maximum that is sustained by the tube's second bending mode of oscillation. In this case the tube also exhibits an intense surge coupled with the second mode of bending having twice the period. For $T = 1.7$ s the incident wavelength matches twice the tube's length ($\lambda = 2L$). Here the pressure bulges become visible, together with a third mode of bending which has the same period as the incident waves. In the proximity of the tube's tuning period an intense bulging occurs, coupled with the third mode of bending. A maximum of $C_W = 2.7$ tube diameters is achieved at $T = 1.17$ s when the wavelength is equal to the tube's length ($\lambda = L$). At this period the bulging and surge are intense and a higher mode of bending begins to form. The three degrees of freedom of the system seem to be coupled so as to deliver the highest energy capture-width obtained for configuration A in these conditions. For smaller incident wave periods the dominant feature is the pressure bulges. The surge and bending modes are not significant, but diffraction and wave breaking along the tube may be observed. This leads to a noticeable decrease in efficiency.

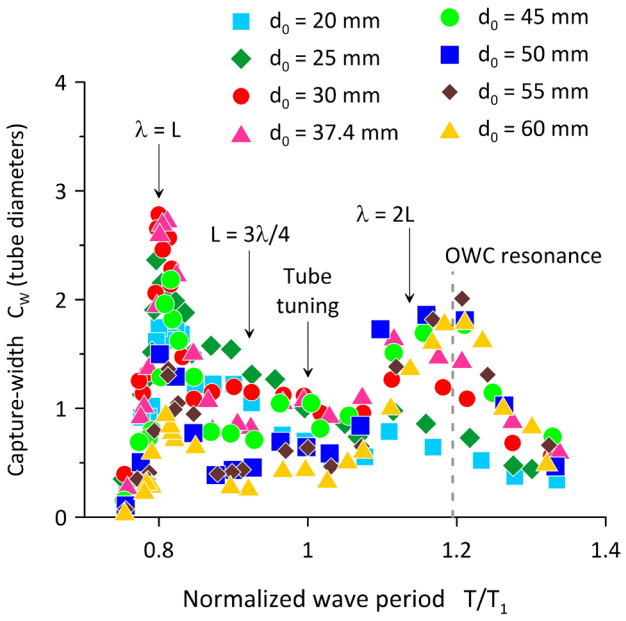

Fig. 12 Capture-width C_W as a function of the normalized wave period T/T_1, for the system with the tube assembled on a jacket platform over uniform depth (configuration A) and all the PTO impedance rates tested

Next, the system's capture-width is compared with existing experimental data obtained by Chaplin et al. (2012) with a long floating distensible-tube fixed at either end, having a linear PTO. The length of the tube is in this case 7 m. The normalized impedance Z previously defined will be used as a measure for comparison of impedance rates between both models. Fig. 13 gives the values of Z for the present 1:20 scale physical model (configuration A), with $Z_{tube} = 24.0\ \text{kPa.m}^{-3}.\text{s}$ and $d_0 = 20, 50, 55$ and 60 mm, and for two of the linear impedances of the 1:25 scale model tested by Chaplin et al. (2012). The incident waves are kept within the range of linearity in the 1:25 scale model and, for the present 1:20 scale model, the characteristics of the incident wave field are presented in table 3.

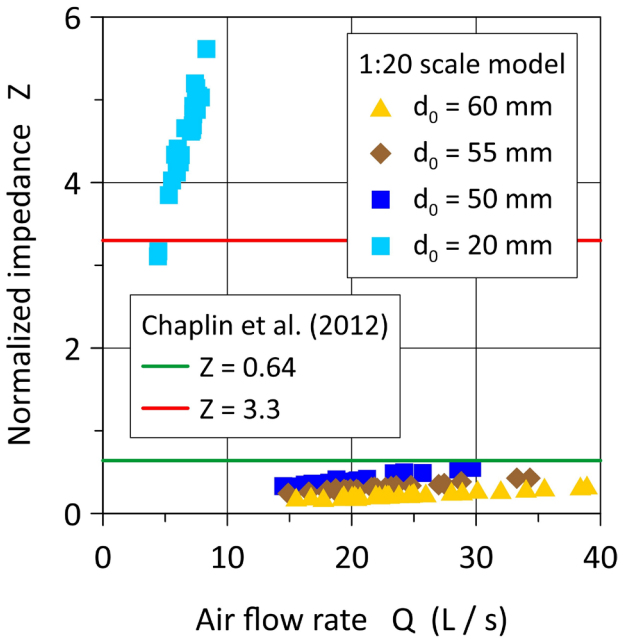

Fig. 13 Normalized impedance Z versus air volume-flow Q, for the present 1:20 scale physical model (configuration A) and for two of the linear impedances of the 1:25 scale model of Chaplin et al. (2012)

In fig. 14 the capture-widths of the 1:20 and 1:25 scale models are shown, for the comparable normalized impedance rates in fig. 13. C_W is here given as a function of the normalized wave period T/T_1, where T_1 is the tube tuning period of the corresponding model. The behaviour is very similar for both models, with the C_W of the 1:20 scale model being slightly shifted relative to the 1:25 experimental data and to the theoretical solution based on Froude-Krylov theory, neglecting hysteresis in the tube. Diffraction has only been observed for very small wave periods. It may be noticed that the maximum capture-width obtained with the two physical models is comparable for the higher impedance rate (fig. 14, right). For the lower impedance rates (fig. 14, left) a higher maximum capture-width is attained by the 1:20 scale model, which is probably due to the coupling of the OWC resonance with the tube bending mode at $\lambda = 2L$. By comparing the two models at full scale, it may be said that OWC-connected shorter tubes are suitable to be excited by sea waves of realistic wavelengths and may attain a better capture when allowed to operate with three degrees of freedom: in surge, bulging and bending modes.

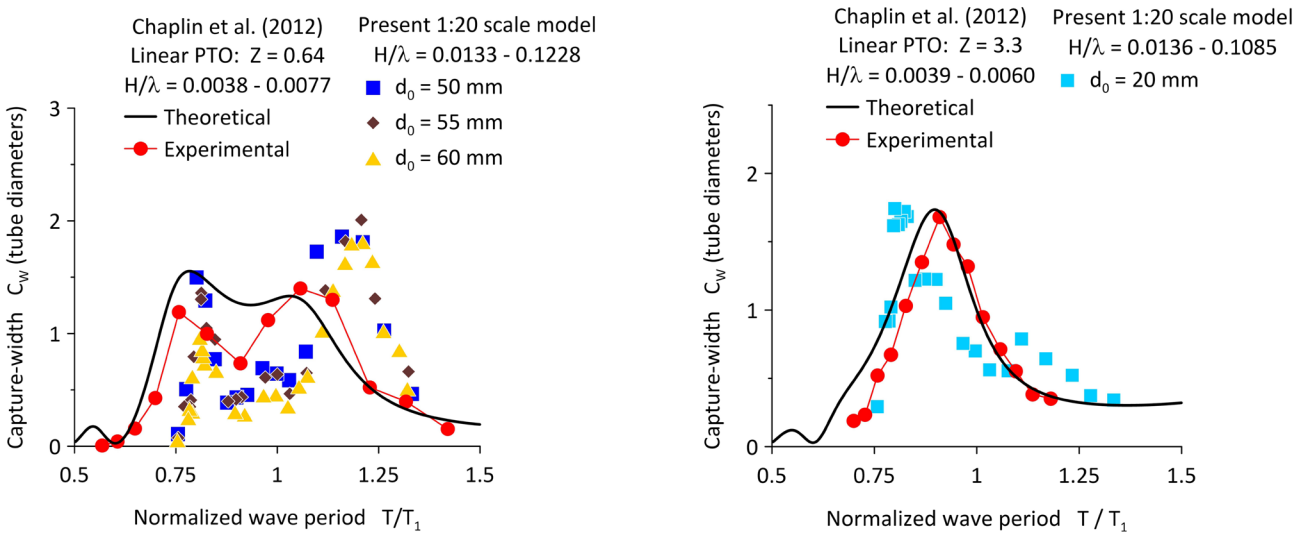

Fig. 14 Capture-width C_W as a function of the normalized wave period T/T_1: a) for the present 1:20 scale model in configuration A, with $Z = 0.19 - 0.55$, and the 1:25 scale model of Chaplin et al. (2012) with constant impedance $Z = 0.64$ (left); b) for the present 1:20 scale model in configuration A, with $Z = 3.11 - 5.61$, and the 1:25 scale model of Chaplin et al. (2012) with constant impedance $Z = 3.30$ (right)

8 The onshore system

It is well known that the existence of a reflecting wall generally improves the efficiency of wave-energy devices significantly (Whittaker and Stewart, 1993). Accordingly, the performance of the distensible-tube wave attenuator was obtained with the system fitted into a sea wall, first over water of constant depth and later over a sloped bottom. The capture-width of the system with a reflecting wall operating over a constant depth bottom (configuration B) is presented in fig. 15 as a function of the normalized wave period T/T_1, for all the impedance rates tested. For long wave periods, above $T = 2.1$ s, there is no tube surge or bulges and a noticeable second bending mode is visible. Here the capture-width is very small. For periods roughly between 1.6 s and 2 s a strong tube surging may be observed. Particularly for $T = 1.97$ s the tube surge is intense and a large bulge is present at its root, when the tube retracts, resulting in a sharp increase of C_W. No bending was detected. The capture-width is maximum near the OWC resonance, at $T = 1.67$ s, reaching $C_W = 2.7$ tube diameters for $d_0 = 30$ mm. A third bending mode with the same period as the surge now seems to be underway. For periods below $T = 1.63$ s the tube surge is not significant. At $T = 1.51$ s, near the predicted bulge wave tuning period ($T = 1.47$ s), the tube bulging is very intense and a third mode of bending develops. Coincidently this is when the tube length is about half the wavelength. The increase in capture-width observed for configuration A in these conditions does not occur in this case. Instead, for $T = 1.24$ s the tube oscillates in bending according to the three-quarter wavelength resonance ($L = 3\lambda/4$). This is very beneficial for the energy capture, an effect that has not been observed at the quarter-wavelength ($L = \lambda/4$). The bulging is again intense and there is no surge. All in all, the introduction of a reflecting barrier improved the capture-width of the system. In configuration B it exceeds one diameter over a wider range of wave periods.

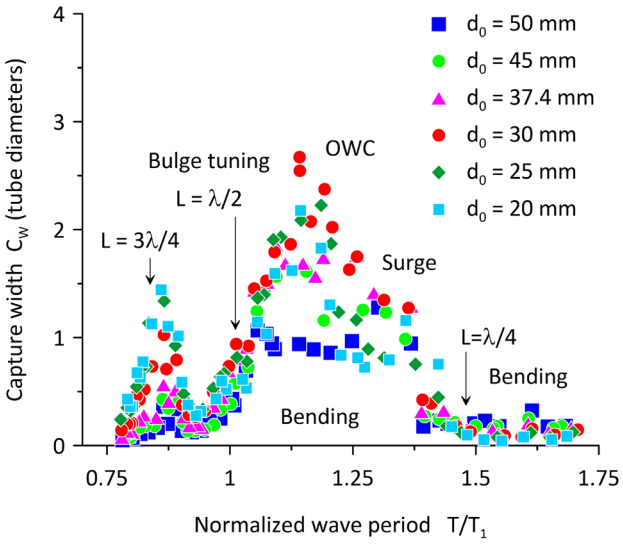

Fig. 15 Capture-width C_W as a function of normalized wave period T/T_1, for the system with the tube fitted into a reflecting wall over uniform depth (configuration B) and all the PTO impedance rates tested.

Next when a sloping bottom is added in front of the vertical barrier (configuration C), significant changes in the wave power capture mechanisms were observed. The corresponding capture-widths are shown in fig. 16 as a function of the normalized wave period T/T_1, for all the impedance rates tested. Likewise in Configuration B, for large wave periods above about $T = 2.15$ s the capture-width approaches zero. There is neither tube surge nor bulges and a noticeable second bending mode is apparent. For periods between 1.6 s and 2 s a strong tube surging has again been observed. Particularly for $T = 1.87$ s the bending mode decays and the tube surge is very intense, associated with the OWC resonance. Bulge waves are visible travelling inside the tube, between the barrier and the nose. Unlike the case of configuration B, the global maximum capture-width is no longer achieved near the OWC resonance. At $T = 1.67$ s it reaches $C_W = 2.27$ tube diameters, where the horizontal length of the sloping bottom is half the wavelength ($X_s = \lambda/2$). No bending is observed, but the tube surging is intense and significant wave bulges now clearly appear. Coincidently, at the tube's tuning period ($T = 1.48$ s) the length of the tube is half the wavelength and C_W reaches about 1. No surge is observed and a third mode of bending appears, together with wave bulges. At $T = 1.31$ s, where the horizontal length of the bottom equals one wavelength ($X_s = \lambda$), the pressure bulges are very intense and the bending becomes fully developed. Here the capture-width is high ($C_W = 1.65$ tube diameters) and there is no surge. For $T = 1.21$ s the tube oscillates in bending according to the three-quarter wavelength resonance ($L = 3\lambda/4$) and the bulges are again intense. This proves advantageous for the energy capture, as a new global maximum of $C_W = 2.5$ tube diameters is reached for $d_0 = 17.2$ mm. This represents an increase of 73.6% in power capture in this region, relative to configuration B, and happens quite close to the period where the incident wavelength equals the horizontal length of the sloped bottom X_s. Nevertheless, a reduction in C_W of about 16.3 % relative to configuration B is observed near the OWC resonance. The increase in power capture observed in configuration C, for $X_s = \lambda$ and $X_s = \lambda/2$, arises from the fact that the sloping bottom bridges the tank walls thereafter forming a perfect channel with two parallel side-walls of length X_s. It is worth noting that the entire length of the tube is in this case comprised within the channel.

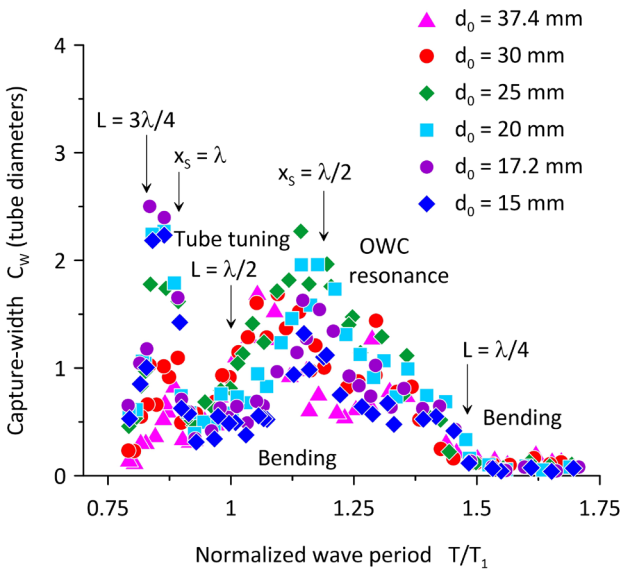

Fig. 16 Capture-width C_W as a function of normalized wave period T/T_1, for the system with the tube fitted in a reflecting barrier over a sloping bottom (configuration C) and all the PTO impedance rates tested

9 Performance improvement by means of a focusing channel

In view of further improving the performance of the onshore system a pair of converging side-walls have been added on top of the sloping bottom (configuration D), as shown in fig. 3. The capture-width C_W obtained for this configuration is presented in fig. 17 as a function of normalized wave period T/T_1, for different PTO orifice diameters. The behaviour observed in this case is similar to that of configuration C. The global maximum capture-width attained is now $C_W = 2.96$ tube diameters for $d_0 = 25$ mm and occurs at $T = 1.76$ s, where $X_s = \lambda/2$. This maximum occurs again quite close the OWC resonant conditions. Coincidently, at the bulge wave tuning period ($T = 1.48$ s) the length of the tube is half the incident wavelength and C_W reaches about 2 tube diameters. The wave bulges are here intense and a third mode of bending develops. A local maximum of $C_W = 1.9$ tube diameters happens at $T = 1.3$ s, where $X_s = \lambda$. Nearby, for $T = 1.25$ s the bulging is intense and the tube oscillates in bending, according to the three-quarter wavelength resonance ($X = 3\lambda/4$), which is very beneficial for the energy capture. The effect introduced by the focusing channel is clearly beneficial, since it raises the capture-width in practically the full range of periods tested. The longitudinal length of the converging side walls X and the horizontal length of the sloping bottom X_s are notably important.

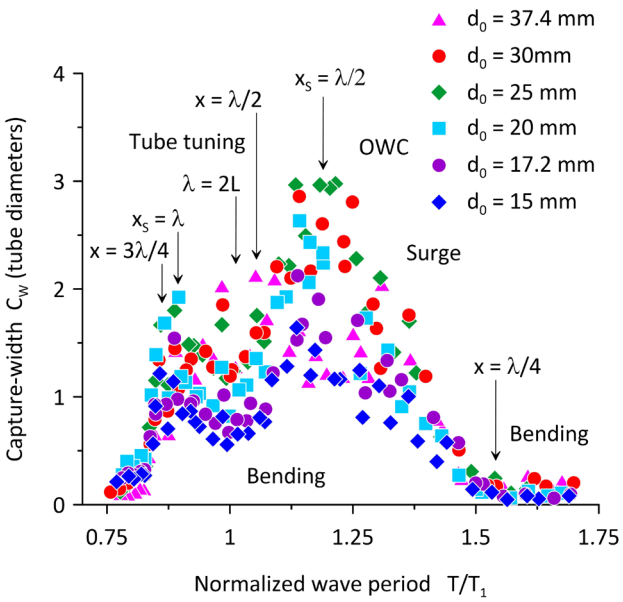

Fig. 17 Capture-width C_W as a function of normalized wave period T/T_1, for the tube operating in a focusing channel (configuration D) and all the PTO impedance rates tested

Fig. 18 depicts a collection of the previous results obtained for all four configurations, as a function of the full-scale significant wave period T_s between 5 and 10 s. It is seen that configuration A is better suited to offshore and nearshore applications where it can reach higher overall energy capture-widths in sea waves between 5 s and 6 s. For longer waves above 6.5 s, which may be found closer to the coast, the addition of a vertical barrier or a focusing channel is notoriously helpful and can bring a significant increase in capture-width. Unexpectedly, the addition of a sloped bottom in front of the vertical barrier does not seem advantageous in the larger periods. Rather, it seems to be beneficial in the higher frequency range.

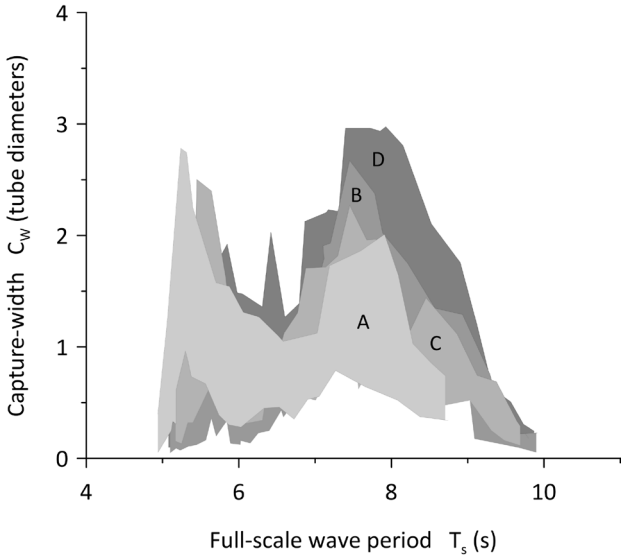

Fig. 18 Comparison of the capture-width C_W as a function of the full-scale significant wave period T_s, achieved with the different configurations: A – distensible tube assembled to a jacket platform; B – Tube fitted in a reflecting wall; C – Tube fitted in a reflecting wall over a sloping bottom; D – Tube operating in a focusing channel

The behaviour of the distensible tube was recorded by a submersible camera during the experiments. A series of images that help in understanding the mechanics behind the system's primary stage of energy conversion in configurations B, C and D are presented in fig. 19. The first horizontal line of images shows the second bending mode of the tube that happens for long waves in each of these three configurations. The second line of images shows the strong surging and bulging that accompanies the maximum C_W, near the OWC natural period. The third line of images depicts the intense bulging near T_1, together with the third mode of bending of the tube. Note that these relevant phenomena occur at different incident wave periods for each of the three configurations.

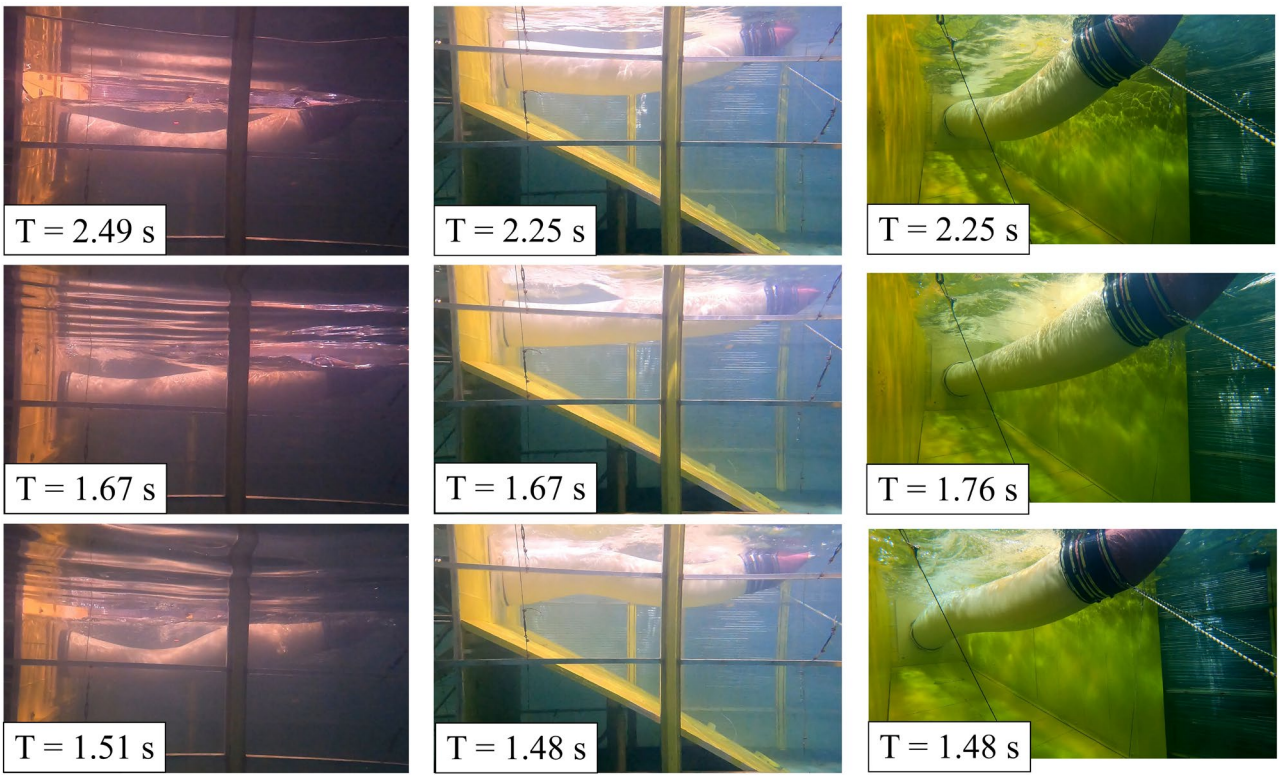

Fig. 19 Distensible tube operating in bending, surge and bulging modes in configurations B (left), C (middle) and D (right), with a PTO orifice of $d_0 = 25$ mm.

10 Comparisons to other OWC systems

In order to better understand the effects of introducing a distensible tube to the forward-bent OWC system, all four configurations were also tested without the distensible tube in place. The results obtained herein are firstly validated against theoretical and experimental predictions existing in the literature for OWCs. Afterwards they are compared with the performance estimates with the tube in place.

10.1 Validation against fixed-draft and bottom-standing OWCs

In fig. 20 the capture-width C_W of the 1:20 scale forward-bent circular OWC in configuration A (see fig. 1a), without the rubber tube in place, is presented for all the PTO impedance rates tested as a function of the normalized wave period T/T_0. The radius to water depth ratio is in this case $r/h = 1/12$ and the values of C_W are here expressed in OWC diameters. These values of C_W are validated against analytical and numerical solutions obtained in linear theory for circular OWCs. They compare with the theoretical predictions provided by Evans and Porter (1997) for a fixed-draft vertical circular OWC with $a/h = 1/4$ (fig. 20, left), showing that at resonance ($T/T_0 = 1$) substantial viscous effects occur in the present forward-bent physical model. Also in fig. 20 (left) a comparison is made with the predictions for a bottom-standing circular OWC given in Deng et al. (2013), for $a/h = 1/5$, where a is in this case the lip submergence. Here the present experimental predictions follow the trend of the numerical solution, but the advantages of the bottom standing OWC with a reflecting C-shaped back-wall under the hollow cylinder become clear, especially for periods bellow resonance. Referring next to fig. 20 (right), comparisons are made with the predictions given by Martins-Rivas and Mei (2009) for a fixed-draft vertical circular OWC of $a/h = 1/5$. The following conclusions may be drawn. At resonance, the experimental results are in agreement

with the predictions in the case of a slimmer OWC of $r/h = 1/4$. They reflect well the trends of the theoretical predictions, keeping in mind the difference in relative OWC diameter and that the numerical model assumes inviscid flow. The higher maximum capture-width attained by the forward-bent OWC is in part due to the smaller ratio $r/h = 1/12$ of the present physical model. At $T/T_0 = 0.69$ and 1 the experimental results confirm the existence of OWC free-surface sloshing, a phenomenon which is illustrated by fig. 21 at the OWC resonance where the displacement is maximum.

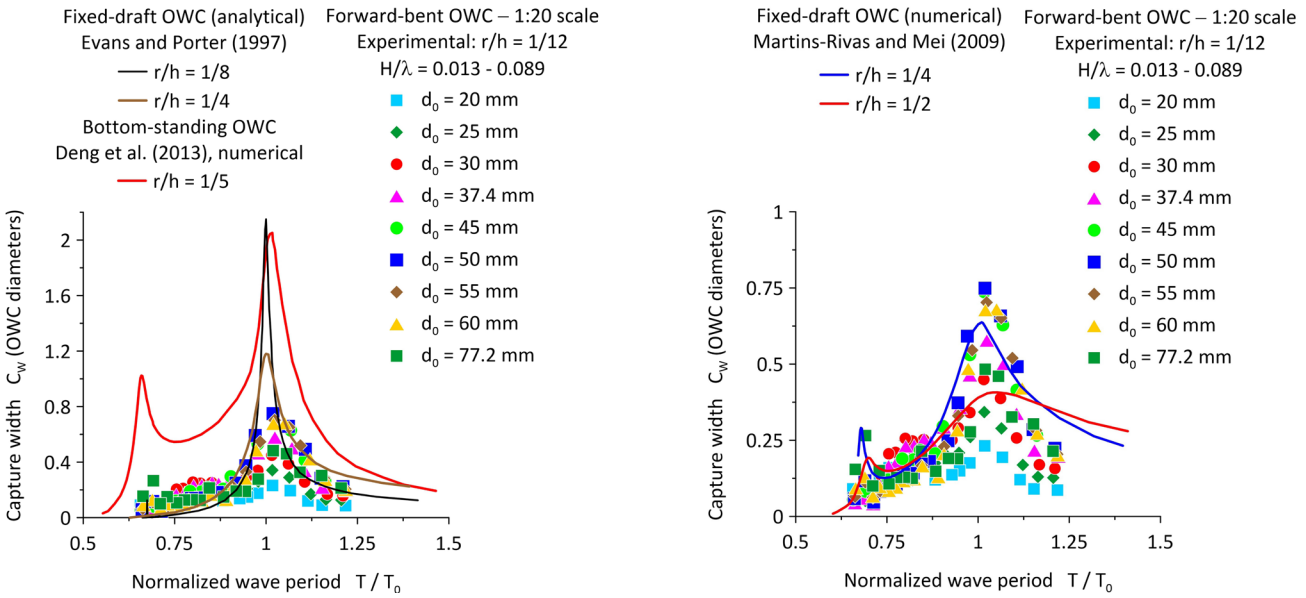

Fig. 20 Comparisons of the capture-width C_W of the forward-bent circular OWC in configuration A, without rubber tube, with the analytical and numerical solutions obtained in linear theory by Evans and Porter (1997) and by Deng et al. (2013) – left – and by Martins-Rivas and Mei (2009) – right

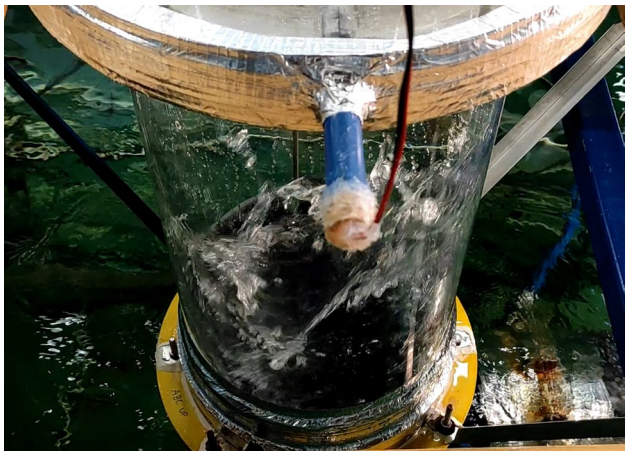

Fig. 21 Sloshing in the OWC free-surface near resonance ($T = 1.65$ s), for the system in configuration A without the distensible tube in place

Once the validation of the forward-bent OWC performance in configuration A has been accomplished, we now proceed to analyse and compare the advantages of configurations B, C and D without the tube in fig. 22. The capture-width is again conveniently presented in OWC diameters, as a function of the non-dimensional wavenumber kh. Fig. 22(a)

concerns the nearshore OWC model, supported by the jacket platform (configuration A). As seen before, the maximum C_W achieved is only 0.75 OWC diameters at the OWC resonance ($kh \approx 3$). Respectively in figs. 22(b) and 22(c) the capture-width in configurations B and C are presented and compared to numerical predictions obtained in linear theory by Deng et al. (2013), for a bottom standing circular OWC of $a/h = 1/5$. The maximum C_W is again achieved at the OWC resonance, reaching now 1.51 and 1.71 OWC diameters for configuration B and configuration C, respectively. Contrarily to when the system was equipped with a distensible tube, configuration C achieves capture-widths greater than those of configuration B. Around the OWC resonance the capture C_W predicted for both these configurations agrees quite well with the numerical solutions given by Deng et al (2013) for the wider OWC; this is particularly true in configuration C. It suggests that the back-wall of the bottom standing OWC of Deng et al. (2013) has a similar reflecting effect as the vertical wall at the mouth of the present forward-bent OWC. Moreover, the addition of a sloping bottom in front of the barrier may result in a Stokes edge-wave near the OWC resonance that slightly broadens the frequency range where C_W is near its maximum. The smaller peaks of capture-width observed at the larger frequencies also follow the trend of the theoretical predictions. They become significantly amplified due to the presence of the sloping bottom, raising from $C_W = 0.34$ in configuration B to $C_W = 0.87$ in configuration C, at $kh = 5$.

Fig. 22(d) shows the capture-width C_W of the forward-bent circular OWC with a focusing channel of $\theta = 37.54°$ flare angle and a 29.1° sloping bottom (configuration D). The maximum C_W is now 3.2 OWC diameters, achieved near resonance when $kh = 1.85$. This maximum value is sustained by the quarter wavelength resonance of the channel, where $X = \lambda/4$, an effect that was not observed when the system had the tube in place (see fig. 17). The behaviour of C_W in this region agrees well with the predictions obtained in linearized theory by Lovas et al. 2010, for a bottom standing circular OWC in an infinite length focusing channel of 90° flare angle at constant depth, particularly for the slimmer OWC with $r/h = 1/4$. The maximum value attained experimentally is however bellow the maximum theoretical C_W; this may on one hand be attributed to the fact that the focusing channel considered has infinite length walls and, on the other hand, to the fact that no viscous losses are taken into account in the theoretical model. Nevertheless, an increase in capture-width of about 4 times relative to configuration A is observed in this case, which is in line with the increase predicted by Lovas et al. (2010). For higher frequencies, two local maximums of C_W appear which are also theoretically predicted. These maxima are amplified due to the focusing channel, augmenting from $C_W = 0.87$ in configuration C to $C_W = 1.40$ in configuration D, at $kh = 5$.

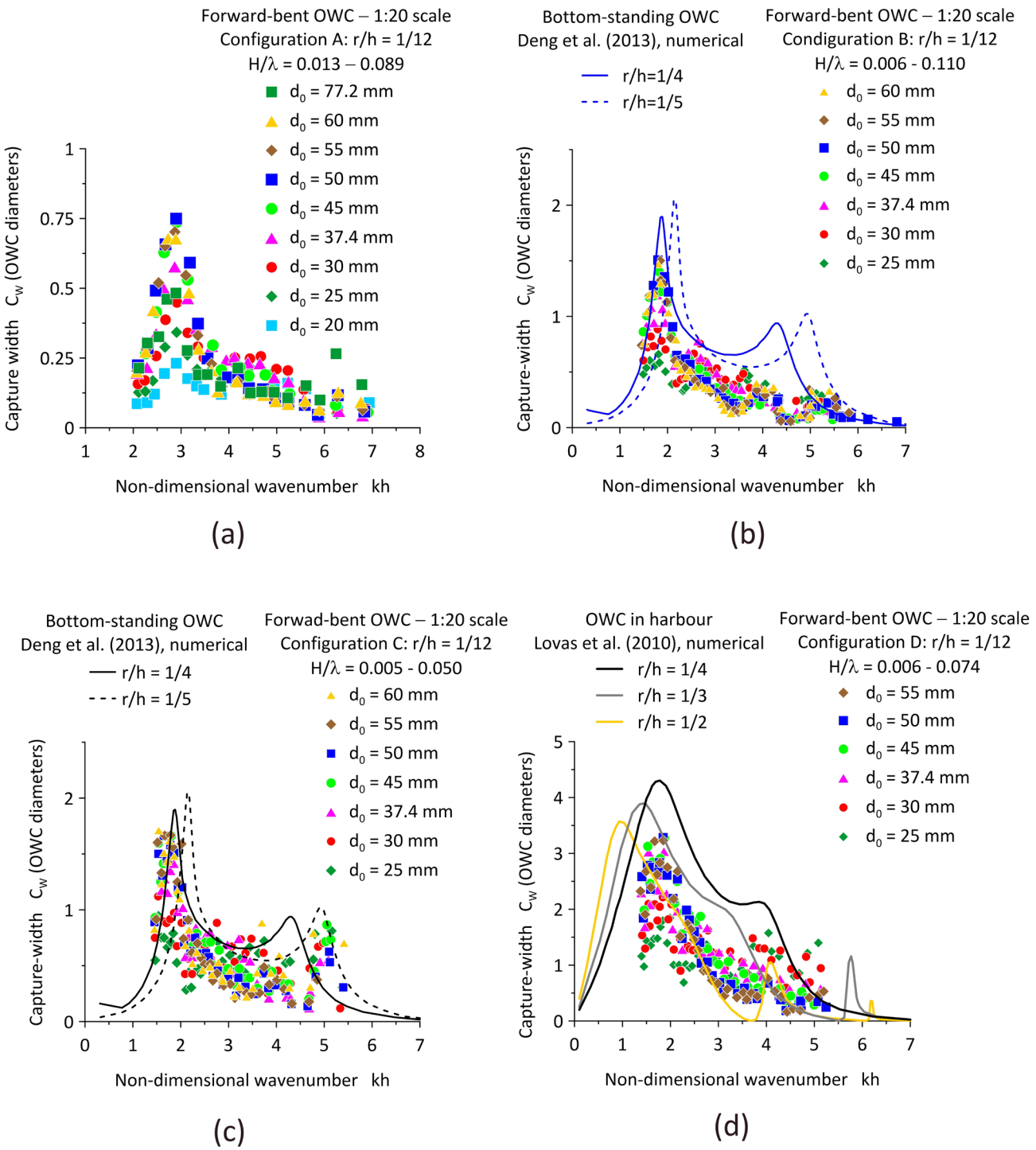

Fig. 22 Comparisons of the capture-width C_W of the forward-bent circular OWC without rubber tube, in configurations A, B, C and D, with the analytical and numerical solutions obtained in linear theory by by Deng et al. (2013) – (b) and (c) – and by Lovas et al. (2010) – (d)

Finally, in fig. 23 a comparison is made between the present 1:20 scale model of a forward-bent circular OWC in configuration D, without the rubber tube, and recent experimental results obtained by David et al. (2018) with a 1:20 scale model of a bottom standing rectangular OWC. In both cases the OWC is placed in a focusing channel, having a flare angle of 37.54° over a sloped bottom for the circular OWC, and a flare angle of 45° in constant depth for the rectangular OWC. The channel length to water-depth ratio is quite similar in both models, being $X/h = 0.97$ in the first case and $X/h = 0.87$ in the second case. The corresponding capture-widths C_W are expressed in OWC-mouth diameters and in caisson mouth

widths, respectively, as a function of the normalized wave period T/T_0. The wave steepness H/λ is also comparable in the two experiments. The maximum capture-width is of the same order in the two models, ranging from 3.25 to 3.5 OWC-mouth widths. However, although the predictions of the two models are in good agreement, the bottom-standing rectangular OWC seems to be better at the lower wave period range, at least for the steeper waves. An important aspect to be noticed is that the sloping bottom in front of the forward-bent OWC possibly produces the same effect as the curved bottom profile inside the rectangular OWC used in David et al. (2018).

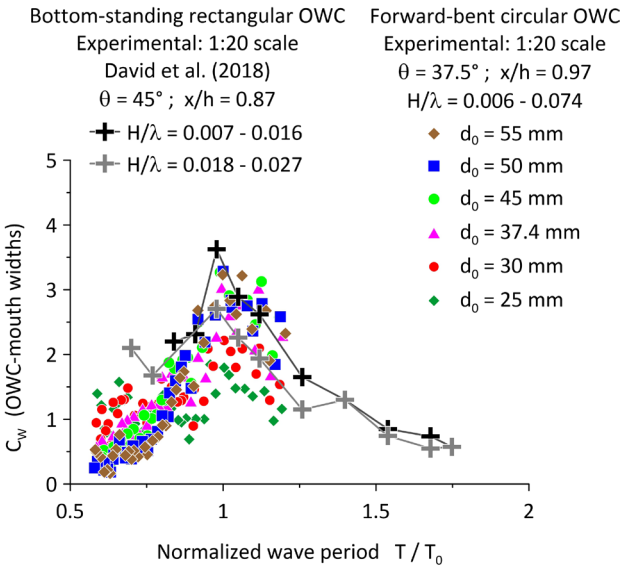

Fig. 23 Comparisons of the capture-width C_W of the present forward-bent circular OWC in configuration D, without rubber tube, with experimental results obtained by David et al. (2018) for a bottom standing rectangular OWC, in a focusing channel of flared walls at constant depth

10.2 Distensible-tube versus forward-bent OWC system

This section aims to compare the performance of the forward-bent OWC system, with and without the distensible tube in position. As shown in fig. 24, in configuration A and undamped conditions the amplification factor is always higher for the system with a distensible tube, relative to the system without one. This is also true for the damped system if comparable impedances are considered. At the OWC resonant period it may become almost 50% higher. Moreover, at the higher wave frequencies ($T = 1.2$ s) the system with a distensible tube presents a second peak in amplification factor of 2.2. These differences in behaviour have a significant impact on the power capture efficiency, as is shown in tables 5 and 6. For the system with and without the distensible tube, these tables summarize the ranges of mean air volume-flow $\bar{Q}$ and mean pressure in the pneumatic chamber $\bar{p}$, together with the mean extracted power at the orifice $\bar{P}$ and the maximum capture-width C_W near the OWC resonance. If only the maximum capture-width is considered, the focusing channel is clearly advantageous both with or without the tube in position. However, a more in-depth analysis is needed.

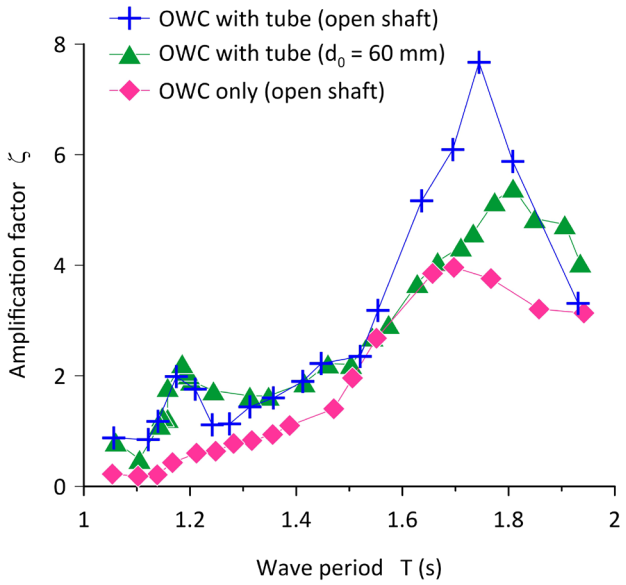

Fig. 24 Amplification factor ζ as a function of incident wave period T, for the system in configuration A with and without the distensible tube in place

Table 5 Operational ranges of the forward-bent OWC model with distensible tube

Config.	$\bar{Q}$ (L/s)	$\bar{p}$ (kPa)	$\bar{P}$ (W)	C_W max
A	4.4–38.9	0.055–1.339	1.10–18.60	2.35
B	1.6–28.4	0.039–1.023	0.11–16.94	3.15
C	1.1–21.0	0.047–1.184	0.12–19.04	2.67
D	1.1–22.6	0.053–1.421	0.13–23.44	3.49

Table 6 Operational ranges of the forward-bent OWC model without distensible tube

Config.	$\bar{Q}$ (L/s)	$\bar{p}$ (kPa)	$\bar{P}$ (W)	C_W max
A	2.1–31.7	0.032–0.286	0.19–4.68	0.75
B	3.1–34.3	0.039–0.691	0.36–15.94	1.51
C	3.7–35.9	0.040–0.701	0.25–16.11	1.71
D	6.1–49.6	0.048–1.096	0.64–31.54	3.22

In fig. 25 (left) a comparison is made between the performance of the system with and without the distensible tube in place, for configuration A. C_W is here referred to the OWC diameter instead of the tube diameter. The range of wave periods T_s considered results from the extrapolation of the wave period T to full-scale, based on the 1:20 scale of the physical model. The envelopes presented cover all the experimental data points obtained. The power capture-width of the system without the tube is $C_W = 0.75$ OWC diameters at the OWC resonance, much lower than the $C_W = 2.35$ OWC diameters obtained when the distensible tube was in place. As it may be observed, the distensible tube wave attenuator in configuration A has a much greater C_W and a larger high-efficiency bandwidth, when compared to a forward-bent circular OWC without a distensible tube. Next, fig. 25 (right) compares the performance of the system operating in a focusing channel (configuration D), with and without the distensible tube. Although both cases present roughly the same maximum capture C_W, the average efficiency over the entire testing bandwidth is in general higher for the distensible tube attenuator. Furthermore, it brings the system's effective period range closer towards the predominant wave climate expected in the Occidental Group of the Azorean islands, where waves with periods between $7 - 8$ s correspond to about 22.7% of the wave observations offshore. The predominant wave height is $H = 1 - 2$ m.

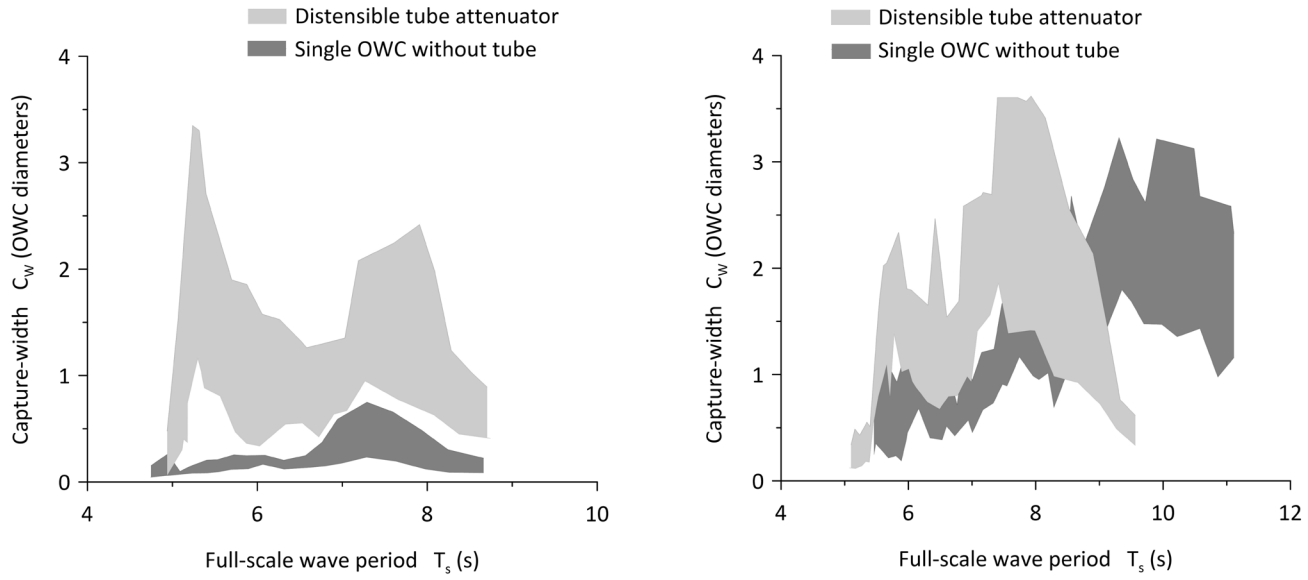

Fig. 25 Envelopes of the capture-width C_W predicted for the system with and without the distensible tube in place in configuration A (left) and configuration D (right), as a function of the full-scale significant wave period T_s

11 Summary of the relevant scaling parameters

Considering a foreseeable prototype that utilizes a rubber tube with about 7 m in diameter, the present model was scaled according to the Froude number $Fr = (2\pi/T)\sqrt{2r/g}$. However, the scaling of the distensible tube also involves the similarity according to the Cauchy number $Ca = \rho U^2/E$. Taking U as the free bulge-wave speed and assuming the same tube material, this parameter may be written $Ca = w/d$, where d is the tube diameter and w it's wall thickness. The inherent hydro-aerodynamic scale-effects, which depend on the size of the model, may lead to an overprediction of the viscous losses and thus incorrect predictions of the device's power capture-width. These losses are associated with friction and turbulence in the internal flows, which for the OWC and distensible tube depend on the Reynolds number $Re_{OWC} = 2r\rho_1\dot{z}/\mu_1$, and for the PTO depend on $Re_{PTO} = 4\rho Q/(\pi\mu d_0)$; $\dot{z}$ denotes the mean velocity of the OWC free-surface. Additionally, they are also related to separated flow and vortex-shedding around the distensible tube in waves, governed by the Keulegan-Carpenter number $Kc = \pi H/d$. Another important parameter that relates the air pressure in the chamber and the inertia forces of the flow across the PTO orifice is the Euler number $Eu = \pi^2 {d_0}^4 \Delta p/(16\rho_1 Q^2)$. All these parameters are gathered in table 7 for the present models and should be carefully considered in order to be able to design a future full scale device.

Table 7 Non-dimensional parameters governing the hydrodynamics of the 1:20 scale model

Config.	Fr	Ca	$Re_{OWC} \times 10^{-4}$	$Re_{PTO} \times 10^{-4}$	Kc	$Eu \times 10^{3}$
A	$0.54 - 1.02$	0.00575	$1.99 - 26.96$	$1.87 - 16.88$	$0.61 - 2.22$	$1.75 - 1.94$
B	$0.43 - 0.95$	0.00570	$0.67 - 14.38$	$0.68 - 4.87$	$0.36 - 1.68$	$1.77 - 2.08$
C	$0.43 - 0.93$	0.00570	$0.53 - 10.62$	$0.64 - 4.76$	$0.33 - 1.38$	$1.75 - 2.09$
D	$0.43 - 0.98$	0.00568	$0.61 - 11.91$	$0.63 - 5.13$	$0.35 - 1.65$	$1.77 - 2.10$

12 Uncertainty analysis

The general theory on the uncertainty analysis of experimental data is well established. Additionally, specific guidelines and recommendations for instrument calibration and uncertainty of experiments in hydrodynamics may be found in the International Towing Tank Conference reports – ITTC (2014, 2017). The present experiments used a 12-bit analogue to digital conversion. After amplification, the output of the wave probes is ± 5 V with a calibration constant of around 0.04 m/V. A random uncertainty of ± 0.3 mm is thus introduced in each water level probe measurement. As the calibration constant of these water level probes varies slightly according to the ambient conditions at the time of the tests, a conservative value of ± 1 mm has been assumed for the water level measurement uncertainty. The output of the pressure transducer is ± 5 V after amplification, with a calibration constant of 1 psi/V, thus resulting in a measured instantaneous pressure uncertainty of ± 33.7 Pa. Reasonable estimates of uncertainties in measurements of volume flow are: ± 0.05 mm for the orifice diameter d_0; ± 0.5 mm for the pneumatic chamber diameter $2r$; ± 0.1°C for the ambient temperature; ± 0.25 mbar for the atmospheric pressure p_0. Finally, Miller (1996) indicates a relative uncertainty of 0.6% for the discharge coefficient C_d and of 0.7% for the expansibility coefficient ε. Consequently, the uncertainty of the mean pressure in the pneumatic chamber, calculated air volume flow, extracted power at the PTO and capture-width were obtained. Table 8 shows the maximum relative errors of the averaged parameters, for the system in configuration A with and without distensible tube, and having a PTO orifice of $d_0 = 50$ mm. As expected, the relative uncertainty is smaller for the system with distensible tube, where the absolute values of the parameters are much larger. A parameter that incorporates the contributions of all measured and calculated properties is the power capture-width, which has been estimated to be within 1.04% of its true value in this case.

Table 8 Maximum relative error (%) of the averaged values, for the system in configuration A with a PTO orifice of $d_0 = 50$ mm

System	Air pressure	Volume flow	Extracted power	Capture-width
OWC + tube	0.66	0.80	0.58	0.88
OWC	2.01	1.83	1.77	1.04

13 Conclusions

Laboratory experiments have been carried out on the operation of a distensible tube wave energy converter similar to the previous Anaconda studied by Farley and Rainey (2006b) and Chaplin et al. (2010, 2012). In the present case the tube was connected to a forward-bent OWC which incorporated a nonlinear power take-off. Firstly the incident waves propagated in deep and intermediate water depth (to simulate nearshore wave conditions), and secondly they were constrained in a channel whose walls and floor converged towards a vertical sea-wall (so as to focus the wave action around the device in onshore conditions). At full-scale the tube would have a length of about 34 m to 43 m, with a pressurized diameter reaching 7 m, and is foreseen to be deployed in Flores and Corvo Islands at the Azores. The forward-bent oscillating water column was also tested in the absence of the distensible tube, in the nearshore and onshore configurations. This led to an indication of any increase in wave power capture-widths that the tube provided.

The device without the sea wall or focusing channel in place reached a maximum wave power capture-width of 2.7 tube diameters (3.3 in OWC diameters). At full scale this would represent a 18.8 m wave front, in sea waves between 5 s and 6 s. Under these conditions the incident wavelength was close to the tube's length and its bending, bulging and surging seem to be coupled in delivering the greatest output. At the OWC's resonance the capture-width reached about 2 tube diameters, a local maximum that was sustained by the tube's oscillation in bending for wave periods between 7 s and 8 s at full scale. The installation of a converging channel led to a 48% increase in power capture about the OWC resonance, while a reflecting barrier on its own provided a 35% increase in the same conditions. Generally, the addition of a slender focusing channel increased the bandwidth over which the capture-width is well above one tube diameter to almost the entire operational range of periods. The focusing channel also made the capture-widths of the OWC with and without the tube comparable.

Considering the incident wave power between 50 kW/m and 110 kW/m available at the coast of Flores and Corvo islands and assuming a conservative value for the capture-width $C_W = 2$ tube diameters, a preliminary estimate of the pneumatic power at the turbine is between 0.7 MW and 1.5 MW. Given the needs in these Islands, two viable solutions could be the production and storage of green hydrogen or the production of fresh water through inverse osmosis. In light of these objectives, the investment and maintenance costs associated with the different solutions studied is a matter for careful consideration in the future. Other relevant questions are the ones related to the device's survival and moorings, as violent motions of the tube occur in waves of shorter periods and larger wave heights.

Statements and Declarations

– The work was partially funded by the Portuguese Foundation for Science and Technology (FCT) and the European Union, within the framework of Programme COMPETE.

– The authors have no conflicting or competing interests to declare that are relevant to the content of this article.

– Ethics approval: Not applicable.

– Consent to participate: Not applicable.

– The authors consent to the publication of this manuscript.

– Availability of data and materials: Not applicable.

– Code availability: Not applicable.

– All authors contributed to the study conception and design. Material preparation, data collection and analysis were performed by F. P. Braga. The first draft of the manuscript was written by A. C. Mendes and all authors commented on previous versions of the manuscript. All authors read and approved the final manuscript.

Nomenclature

A_0 orifice area

a	OWC mouth/tube stern submergence
b	wave-tank width
b'	Reynolds number correction factor
C_d	orifice discharge coefficient
C_0	impedance coefficient
C_W	power capture-width
C_∞	discharge coefficient for infinite Reynolds number
c	incident wave celerity
D	tube distensibility
d	pressurized rubber tube diameter
d_0	orifice diameter
E	Young's modulus
e	gap between channel mouth and tank side-walls
H	incident wave height
h	water depth in the tank
h_0	pressure head in the shaft
h_1	height of pneumatic chamber
k	fundamental wave number
L	rubber tube length
l	OWC length
$\dot{m}$	mass flow-rate across orifice
P	extracted power at the PTO
P_i	incident wave power
p	air pressure in the pneumatic chamber
p_0	atmospheric pressure
p^*	air pressure upstream of the orifice
Q	volume flow-rate of air across orifice
q	maximum instantaneous air volume flow
Re	Reynolds number
$\mathrm{Re_u}$	Reynolds number upstream of the orifice
r	internal radius of pneumatic chamber
T	incident wave period
T_0	OWC's natural period
T_1	tube's tuning period
T_S	full-scale significant wave period
t	time
U	bulge wave speed
Ur	Ursell number
w	tube wall-thickness
X	longitudinal length of the focusing channel
X_S	horizontal length of the sloped bottom
Z	normalized impedance
$\bar{Z}_{PTO}$	mean PTO impedance
Z_{tube}	distensible tube impedance
$\dot{z}$	mean velocity of the OWC free-surface
β	orifice diameter to upstream diameter ratio
γ	specific heat ratio of air
Δp	differential pressure
ε	expansibility factor

ζ amplification factor
η water surface displacement in shaft
θ flare angle of the focusing channel
λ incident wavelength
μ absolute viscosity of air
μ_1 absolute viscosity of water
ρ mass density of air passing through orifice
ρ_1 mass density of water
ρ^* mass density of air upstream of orifice

References

Ambli N, Bønke K, Malmo O, Reitan A (1982) The Kvaerner Multiresonant OWC. In: Proc. of the 2nd International Symposium on Wave Energy Utilization, pp. 275-296, Throndheim.

ASME (2004) Measurement of Fluid Flow in Pipes Using Orifice, Nozzle and Venturi. ASME MFC-3M-2004, Revision of ASME MFC-3M-1989 (R1995), American National Standard issued by the American Society of Mechanical Engineers (ASME), New York.

Caires S, Sterl A, Komen G, Swail V (2013) Global Wave Climatology Atlas. Koninklijk Nederlands Meteorologisch Instituut, Ministry of Infrastructure and Environment, De Bilt.

Chaplin JR, Farley FJM, Rainey RCT (2007a) Power Conversion in the Anaconda WEC. In: Proc. International Workshop on Water Waves and Floating Bodies, 4 pp., Plitvice.

Chaplin JR, Farley FJM, Prentice ME, Rainey RCT, Rimmer SJ, Roach AT. (2007b) Development of the Anaconda All-Rubber WEC. In: Proc. of the 7th European Wave and Tidal Energy Conference, 13 pp., Porto.

Chaplin JR, Farley FJM, Hearn GE, Heller V, Mendes AC (2010) Hydrodynamic Performance of the Anaconda Wavepower Device. In: Proc. HYDRALAB III Stakeholder Dissemination Meeting, Hannover.

Chaplin JR, Heller V, Farley FJM, Hearn GE, Rainey RCT (2012) Laboratory Testing the Anaconda. Philos Trans R Soc A 370(1959): 403-424. https://doi.org/10.1098/rsta.2011.0256

Count BM, Evans DV (1984). The Influence of Projecting Sidewalls on the Hydrodynamic performance of Wave-energy Devices. J Fluid Mech 145:361-376. https://doi.org/10.1017/S0022112084002962

David DR, Vallam S, Annamalaisamy SS (2018) Effect of Harbour Walls on the Efficiency of an Oscillating Water Column. J Waterw Port Coast Ocean Eng 144(2):1-16. https://doi.org/10.1061/(ASCE)WW.1943-5460.0000429

Deng Z, Huang Z, Law AWK (2013) Wave Power Extraction by an Axisymmetric-oscillating-water-column Converter Supported by a Coaxial Tube-sector-shaped Structure. Appl Ocean Res 42: 114-123. https://doi.org/10.1016/j.apor.2013.05.006

Deng Z, Huang Z, Law AWK (2014) Wave Power Extraction from a Bottom-Mounted Oscillating Water Column Converter with V-Shaped Channel. Proc R Soc A 470:20140074. https://doi.org/10.1098/rspa.2014.0074

Evans DV, Porter R. (1997) Efficient Calculation of Hydrodynamic Properties of OWC-type Devices. J Offshore Mech Arct Eng 119(4): 210–218. https://doi.org/10.1115/1.2829098

Falcão AFO (2010) Wave Energy Utilization – A Review of the Technologies. Renew Sustain Energy Rev 14(3):899-918. https://doi.org/10.1016/j.rser.2009.11.003

Falcão AFO, Henriques JCC (2016): Oscillating-water-column Wave Energy Converters and Air Turbines: A review. Renew Energy 85:1391–1424. https://doi.org/10.1016/j.renene.2015.07.086

Farley FJM, Rainey RCT (2006a) Distensible Tube Wave Energy Converter. British Patent Nº. GB 2434840.

Farley FJM, Rainey RCT (2006b) Radical Design Options for Wave-Profiling Wave Energy Converters. In: Proc. of the 21st International Workshop on Water Waves and Floating Bodies, 4 pp., Loughborough.

Farley FJM, Rainey RCT, Chaplin JR (2012) Rubber Tubes in the Sea. Philos Trans R Soc A 370(1959):381-402. https://doi.org/10.1098/rsta.2011.0193

Hawthorne WR (1961) The Early Development of the Dracone Flexible Barge. Proc Inst Mech Eng 175(1):52-83. https://doi.org/10.1243/PIME_PROC_1961_175_011_02

ITTC (2014) Recommended Procedures and Guidelines, section 7.5-02-01-01 − Guide to the Expression of Uncertainty in Experimental Hydrodynamics. International Towing Tank Conference. https://ittc.info/media/4046/75-02-01-01.pdf. Accessed 27 June 2021

ITTC (2017) Recommended Procedures and Guidelines, section 7.5-01-03-01 – Uncertainty Analysis, Instrument Calibration. International Towing Tank Conference. https://www.ittc.info/media/9575/75-01-03-01.pdf. Accessed 27 June 2021

Lighthill J (1978) Waves in Fluids. Cambridge University Press, Cambridge.

Lovas S, Mei CC, Liu Y (2010) Oscillating Water Column at a Coastal Corner for Wave Power Extraction. Appl Ocean Res 32(3):267–283. https://doi.org/10.1016/j.apor.2010.06.004

Magagna D (2020) Ocean Energy – Technology Development Report. EUR 30509 EN, Publications Office of the European Union, Luxembourg. https://doi.org/10.2760/102596

Malmo O, Reitan A (1985) Wave-power Absorption by an Oscillating Water Column in a Channel. J Fluid Mech 158:153-175. https://doi.org/10.1017/S0022112085002592

Malmo O, Reitan A (1986) Wave-power Absorption by an Oscillating Water Column in a Reflecting Wall. Appl Ocean Res 8(1):42-48. https://doi.org/10.1016/S0141-1187(86)80030-X

Mansard EPD, Funke ER (1980) The Measurement of Incident and Reflected Spectra Using a Least Squares Method. In: Proc. of the 17th International Conference on Coastal Engineering (ICCE), Sydney. https://doi.org/10.9753/icce.v17.8

Martins-Rivas H, Mei CC (2009) Wave Power Extraction from an Oscillating Water Column at the Tip of a Breakwater. J Fluid Mech 626:395-414. https://doi.org/10.1017/S0022112009005990

Matos A, Madeira F, Fortes CJEM, Didier E, Poseiro P, Jacob J (2015) Wave Energy at Azores Islands. In: Proceedings of the 7th International Short Course and Conference on Applied Coastal Research, Florence.

McIver P, Evans DV (1988) An Approximate Theory for the Performance of a Number of Wave-Energy Devices Set into a Reflecting Wall. App Ocean Res 10(2):58-65. https://doi.org/10.1016/S0141-1187(88)80032-4

Mendes AC, Monteiro WML (2007) Energy-Loss Assessment for OWC Wave Power Systems in Off-Design working Conditions. In: Proc. of the 17th International Offshore and Polar Engineering Conference, Paper ISOPE-I-07-009, Lisbon.

Mendes AC, Paredes LMA, Gil FAS, Chaplin JR (2014) Small-scale Model Tests of a Rubber-tube Wave Energy Converter with Pneumatic Power Take-off. In: Proc. of the ASME 33rd International Conference on Ocean, Offshore and Arctic Engineering, Paper OMAE2014-23452, San Francisco. https://doi.org/10.1115/OMAE2014-23452

Mendes AC, Braga FP, Paredes LMA, Chaplin JR (2017) Performance Assessment of the Anaconda WEC in Regular Waves at 1:50 Model Scale. In: Proceedings of the 36th International Conference on Ocean, Offshore and Arctic Engineering, Paper OMAE2017-61478, Trondheim. https://doi.org/10.1115/OMAE2017-61478

Mendes AC, Braga FP, Chaplin JR (2020) Wavetank Tests With a 1:20 Scale Model of a Distensible Tube Device for Wave Power Harnessing in the Azores. In: Proceedings of the ASME 2020 38th International Conference on Ocean, Offshore and Arctic Engineering, OMAE2020-18176, Fort Lauderdale. https://doi.org/10.1115/OMAE2020-18176

Miller RW (1996) Flow Measurement Engineering Handbook. McGraw-Hill Publications, 3rd ed., New York.

Reader-Harris M. (2015) Orifice Plates and Venturi Tubes. Springer International Publishing, Switzerland.

Salter S (2016) Wave energy – Nostalgic Ramblings, Future Hopes and Heretical Suggestions. J Ocean Eng Mar Energy 2:399-428. https://doi.org/10.1007/s40722-016-0057-3

Sarmento AJNA, Brito e Melo A, Pontes MT (2003) The Influence of the Wave Climate on the Design and Annual Production of Electricity by OWC Wave Power Plants. J Offshore Mech Arct Eng 125(2):139-144. https://doi.org/10.1115/1.1555112

Tseng R, Wu R, Huang C (2000) Model Study of a Shoreline Wave-power System. Ocean Eng 27(8):801-821. https://doi.org/10.1016/S0029-8018(99)00028-1

Whittaker TJT, Stewart TP (1993) An Experimental Study of Nearshore and Shoreline Oscillating Water Columns with Harbors. In: Proceedings of the 1993 European Wave Energy Symposium, Paper D2, Edinburgh.